

Numerical analysis of gas–particle two-phase flows

By R. ISHII, Y. UMEDA AND M. YUHI

Department of Aeronautics, Kyoto University, Kyoto 606, Japan

(Received 15 April 1988 and in revised form 20 October 1988)

This paper is concerned with a numerical analysis of axisymmetric gas–particle two-phase flows. Underexpanded supersonic free-jet flows and supersonic flows around a truncated cylinder of gas–particle mixtures are solved numerically on the super computer Fujitsu VP-400. The gas phase is treated as a continuum medium, and the particle phase is treated partly as a discrete one. The particle cloud is divided into a large number of small clouds. In each cloud, the particles are approximated to have the same velocity and temperature. The particle flow field is obtained by following these individual clouds separately in the whole computational domain. In estimating the momentum and heat transfer rates from the particle phase to the gas phase, the contributions from these clouds are averaged over some volume whose characteristic length is small compared with the characteristic length of the flow field but large compared with that of the clouds. The results so obtained reveal that the flow characteristics of the gas–particle mixtures are widely different from those of the dust-free gas at many points.

1. Introduction

In many analyses of gas–particle two-phase flows, the two-fluid model has been used. In this model, the gas and the particle phases are treated as separate media, and both phases exchange their momenta and energies through the particle surfaces by the gas viscosity and heat conduction (Carrier 1958; Marble 1963; Rudinger 1969; Schmitt-von Schubert 1969).

When the Knudsen number K_n , the ratio of the mean free path of the gas molecule $\bar{\lambda}$ to the characteristic length of the flow field \bar{L} , is sufficiently small, it is commonly accepted that the gas phase can be treated as a continuum medium. The particle phase can be treated as continuum medium when the mean particle spacing \bar{l}_p is sufficiently small compared with the characteristic length \bar{L} . In many practical situations where the conditions $K_n \ll 1$ and $\bar{l}_p/\bar{L} \ll 1$ are satisfied, both the gas and the particle phases can be treated as continuum media.

Recently, Crowe (1982) proposed a new criterion for diluteness of gas–particle suspensions. He categorized the flow of a gas–particle mixture according to the significance of particle–particle collisions on particle motion. The dilute and dense categories for a gas–particle flow are directly analogous to the free-molecule and continuum flow regimes of a single (gas)-phase fluid. Here, the parameter corresponding to the Knudsen number is the Stokes number based on the distance a particle travels between collisions. Consider a particle which has a velocity $\Delta\bar{u}_p$ relative to the gas. Then the particle will travel a distance of about $\Delta\bar{u}_p \bar{t}_p$ before it stops in the coordinate system moving with the gas, where \bar{t}_p is the aerodynamic relaxation time of the particle velocity. If this distance is small compared with the

distance $\bar{\lambda}_p$ travelled between particle–particle collisions in the same coordinate system, then one can regard the particle cloud as dilute.

Crowe's criterion is, however, not always practical and appropriate in general. If we consider spherical particles of uniform size with constant material density, it will be almost impossible for nearby particles to attain velocities appreciably different from each other in the flow field under the condition $\bar{l}_p/L \ll 1$ unless external forces are exerted on the particles. This means that under this condition particle–particle collisions will not occur or will be negligible for the particle–phase flow in many gas–particle two-phase flows. As was discussed by Crowe (1982), and will also be shown in the present study, there are some situations where intersections of particle clouds can occur in the flow field. In such cases, the significance of particle–particle collisions for the flow should first be measured using the ratio $\bar{\lambda}_p/L$. It is important to point out that the particles may be treated as a continuum even in the limit of infinite dilution (Marble 1970).

Here we shall discuss a more precise criterion for the diluteness of gas–particle suspensions. In general, the material density $\bar{\rho}_{mp}$ of a normal solid or liquid particle is larger by a magnitude of 10^3 than that of a gas $\bar{\rho}$. The volume fraction ϵ_p is given by $\nu\bar{\rho}/\bar{\rho}_{mp}$, where ν is the mass loading ratio of the particles. If the particle mean free path $\bar{\lambda}_p$ is $\bar{l}_p/\epsilon_p^{\frac{2}{3}}$, then $\bar{\lambda}_p/L = (\bar{l}_p/L)/\epsilon_p^{\frac{2}{3}}$. Therefore, if $\bar{l}_p/L = O(\epsilon_p^{\frac{2}{3}})$, then $\bar{\lambda}_p/L = O(1)$ and the gas–particle mixture can be treated as dilute. In other words, if $\nu = O(1)$, $\bar{l}_p/L = O(10^{-2})$ is a sufficient condition for the particle phase to be dilute. In exact terms, the particle mean free path $\bar{\lambda}_p$ depends on the relative velocity of crossing particles. It will, however, be reasonable to assume that $\bar{\lambda}_p = O(\bar{l}_p/\epsilon_p^{\frac{2}{3}})$, and then the above discussion will generally be valid.

In the present paper, we consider a gas–particle mixture under the conditions that $K_n \ll 1$, $\bar{l}_p/L \ll 1$ (or more precisely $\bar{l}_p/L = O(\epsilon_p^{\frac{2}{3}})$) and $\nu = O(1)$, and the particles are assumed to be spheres of uniform size and material. Based on the above discussions, the present gas–particle mixture is obviously a 'dilute' one.

In continuum gas dynamics, the basic thermodynamic properties of the gas are the pressure, the density and the temperature. In a dilute particle phase, there is no particle pressure. Information transfer in a gas phase is through pressure waves which move in all directions, while information travels along particle trajectories in a particle phase. This is the most significant difference between the two phases. Since a solid or a liquid particle has a very much larger mass than a gas molecule, the particle streamlines do not always coincide with the gas streamlines even in a steady flow (Ishii & Umeda 1987). Moreover, it often happens that the particle cloud breaks up into small subclouds and also particle-free regions appear in the flow field.

When a flow is highly unsteady, disintegration of a particle cloud usually produces some small subclouds. These subclouds can in turn coalesce or collide with each other in some different flow regions. It should be stressed, however, that the collision between small particle clouds does not always result in the direct collision between particles in the clouds. As was discussed previously, except in some extreme situations particle–particle collisions can be neglected even when the collision between small particle clouds occurs, if the particle mass loading ratio ν is $O(1)$ and hence the particle volume fraction ϵ_p is negligibly small.

Mathematically, the collision between particle clouds leads to multivalued fields of the particle phase at the colliding points in the flow region. In the present analysis, therefore, the particle phase is treated partly as a discrete one. The whole particle cloud is divided into a large number of small clouds. In each cloud, it is assumed that the particles have the same velocity and temperature. The particle flow field is solved by following the behaviour of all the clouds in the flow field. In estimating the

momentum and the energy transfer rates from the particle phase to the gas phase, the contributions from the clouds are averaged over some appropriate volume. The cross-sections of the clouds and the averaging volume are chosen so that the conditions $\bar{L}_p^2 \ll \Delta \bar{S}_p \ll \bar{S}_p \ll \bar{L}^2$ are satisfied, where $\Delta \bar{S}_p$ and \bar{S}_p are the cross-sectional areas of the clouds and the averaging volume, respectively.

First, one-phase flows of sonic jets and those around a truncated cylinder are described. Second, the flow behaviours of the particles in the gas flows are investigated for the limiting case where $\nu \rightarrow 0$. Finally, the two-phase results are presented for $\nu = 0.3$ and detailed comparison between the one-phase and two-phase results will be made to clarify the effects of the presence of particles on the flow fields.† The calculations have been performed on Fujitsu VP-400 super computer at the Data Processing Center of Kyoto University. The theoretical maximum speed of VP-400 is 1.7 GFLOPS (billion floating-point operations per second) and its main memory is 256 MB (megabytes) in capacity.

2. Governing equations

Although some of the important assumptions introduced in the present analysis have been discussed in the previous section, here we summarize them with the other important assumptions that will be used here (Ishii & Matsuhisa 1983).

- (i) No phase change takes place.
- (ii) The gas is inviscid except for its interaction with the particles.
- (iii) The gas is a continuum perfect gas with constant composition and constant specific heats.
- (iv) The volume occupied by the particles is negligible and the mean particle spacing is much smaller than the smallest scale of flow structure.
- (v) The thermal and Brownian motion of the particles is negligible.
- (vi) The particles do not interact with each other.
- (vii) The particles are solid or liquid spheres with a uniform diameter and a constant material density.
- (viii) The particles have a constant specific heat and uniform internal temperature.

Here we introduce non-dimensional quantities:

$$\left. \begin{aligned} x &= \frac{\bar{x}}{\bar{L}}, & y &= \frac{\bar{y}}{\bar{L}}, & t &= \frac{\bar{c}_r \bar{t}}{\bar{L}}, & \rho &= \frac{\bar{\rho}}{\bar{\rho}_r}, & p &= \frac{\bar{p}}{\bar{p}_r}, \\ u &= \frac{\bar{u}}{\bar{c}_r}, & v &= \frac{\bar{v}}{\bar{c}_r}, & T &= \frac{\bar{T}}{\bar{T}_r}, & c &= \frac{\bar{c}}{\bar{c}_r}, \\ x_p &= \frac{\bar{x}_p}{\bar{L}}, & y_p &= \frac{\bar{y}_p}{\bar{L}}, & u_p &= \frac{\bar{u}_p}{\bar{c}_r}, & v_p &= \frac{\bar{v}_p}{\bar{c}_r}, & T_p &= \frac{\bar{T}_p}{\bar{T}_r}, \end{aligned} \right\} \quad (1)$$

and also for later convenience

$$f_p = \frac{C_D}{C_{DS}}, \quad g_p = \frac{N_u}{N_{uS}}, \quad (2)$$

$$\Gamma_r = \frac{\bar{\tau}_A}{\bar{\tau}_F}, \quad \Gamma_\rho = \frac{\bar{\rho}_{mp}}{\bar{\rho}_r}, \quad \nu_r = \frac{\bar{\rho}_{pr}}{\bar{\rho}_r}, \quad (3)$$

$$\gamma = \frac{\bar{C}_{pg}}{\bar{C}_{vg}}, \quad \theta = \frac{\bar{C}_{pp}}{\bar{C}_{pg}}, \quad (4)$$

† Copies of more detailed numerical results may be obtained on request from either the authors or the Editor.

where t , x and y are the time, axial distance and radial distance, respectively; u , v , p , T and c are the axial velocity, radial velocity, pressure, temperature and speed of sound of the gas, respectively. The subscripts p and r denote particles and reference conditions, respectively, and overbars denote the dimensional quantities. The location of a particle at a time t is denoted by (x_p, y_p) . The quantities \bar{C}_{vg} , and \bar{C}_{pg} are the specific heats at constant volume and pressure of the gas, respectively, \bar{C}_{pp} is the specific heat of the particle material, γ the ratio of specific heats of the gas, C_D the particle drag coefficient, N_u the Nusselt number and $\bar{\rho}_{mp}$ the material density of the particles. The subscript S denotes the Stokes flow. The non-dimensional parameter Γ_r is defined as a ratio of the aerodynamic response time of a particle assuming the Stokes drag law, $\bar{\tau}_A$, to a characteristic time of the flow field, $\bar{\tau}_F$. These are defined as

$$\bar{\tau}_A = \frac{\bar{\rho}_{mp}(2\bar{r}_p)^2}{18\bar{\mu}}, \quad \bar{\tau}_F = \frac{\bar{L}}{\bar{c}_r}, \quad (5)$$

where \bar{r}_p is the particle radius and $\bar{\mu}$ is the gas viscosity. The parameters f_p and g_p are the modifying factors of the drag coefficient and the Nusselt number for the Stokes flow, respectively.

In the present analysis, the gas viscosity $\bar{\mu}$ is given by

$$\bar{\mu} = \bar{\mu}_r \left(\frac{\bar{T}}{\bar{T}_r} \right)^\delta, \quad (6)$$

where δ is a constant. The particle drag coefficient C_D and the Nusselt number N_u used here are those given by Henderson (1976) and Carlson & Hoglund (1973). In this drag coefficient, virtual mass force, pressure gradient force, Basset force and side force (Saffman 1965) are all neglected. As was reported by Maxey & Riley (1983), the neglect of these forces is justified, because $\Gamma_p (= \bar{\rho}_{mp}/\bar{\rho}_r)$ is assumed to be in the range 10^3 – 10^4 for a typical gas–solid flow system in this study. The effects of the volume fraction on the particle drag are also neglected (Tam 1969) on the basis of assumption (iv). The force exerted on a particle includes rarefaction, inertial and compressibility effects and also that of a temperature difference between the particle and the gas. The flow regimes to which the present drag force is applicable are continuum, slip, transition and free-molecular flows at particle Mach numbers up to 6, and at particle Reynolds number up to laminar–turbulent transition.

2.1. Particle phase

We consider the motion of a particle. The motion is controlled by Newton's law. Denoting the particle location by $(x_p(t), y_p(t))$, we have

$$\frac{dU_{pi}}{dt} = I_{pi}, \quad (7)$$

where

$$U_p = \begin{bmatrix} x_p \\ y_p \\ u_p \\ v_p \\ T_p \end{bmatrix}, \quad I_p = \begin{bmatrix} u_p \\ v_p \\ A_p(u - u_p) \\ A_p(v - v_p) \\ B_p(T - T_p) \end{bmatrix}. \quad (8)$$

Here the particles are labelled by subscripts i ($i = 1, 2, 3, \dots$). The last is the

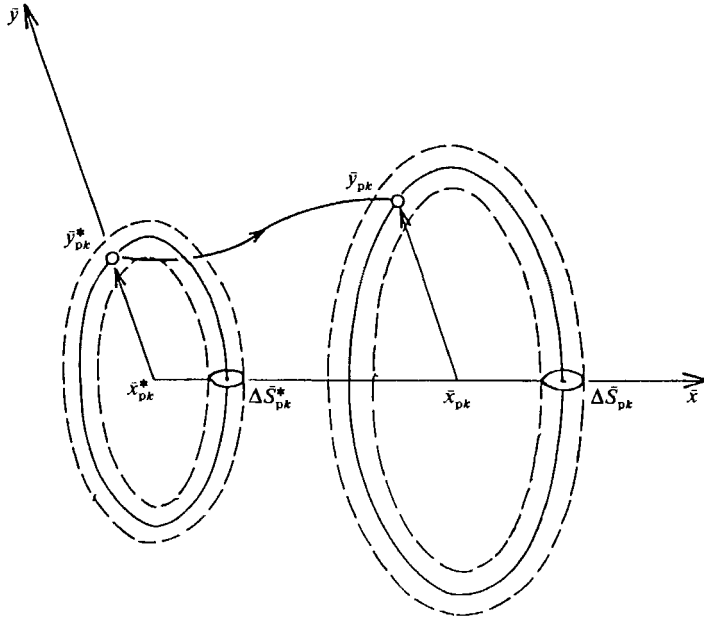


FIGURE 1. A cloud of particles in the physical space. Since the flow is axisymmetric, the particle cloud in the physical space is a ring cloud. The number of particles contained in the k -cloud is given by $2\pi\bar{y}_{pk}\bar{N}_{pk}$.

relaxation equation of the particle temperature T_p . The parameters A_p and B_p are defined by

$$A_p = \frac{f_p}{\Gamma_r}, \quad B_p = \frac{2g_p}{3P_r\theta\Gamma_r}, \quad (9)$$

where P_r is the Prandtl number of the gas. These equations are applicable when the particle velocity is a non-fluctuating function of time and position in the gas (Marble 1970).

In principle, the particle flow field is solved by following all the particles using the above equations. In practice, however, there are too many particles in a flow field to do this, so instead we consider a large but tractable number of small clouds, which are axially symmetric. Their cross-sections are denoted by ΔS_{pk} ($= \Delta\bar{S}_{pk}/\bar{L}^2$). The centre of ΔS_{pk} is designated by $(x_{pk}(t), y_{pk}(t))$ ($k = 1, 2, 3, \dots$). ΔS_{pk} must be taken to be so small that the particles contained in a cloud can be approximated to have the same velocity and temperature. So ΔS_{pk} must satisfy $\Delta S_{pk} \ll (\Delta L)^2$, where ΔL ($= \Delta\bar{L}/\bar{L}$) is the smallest scale of the flow structure; namely there should be a sufficient number of clouds contained in $(\Delta L)^2$. When a cloud is injected into a flow field at a time t^* at a point $(x_{pk}(t^*), y_{pk}(t^*))$, the positions of all the particles in the cloud at an arbitrary time t are represented by the point $(x_{pk}(t), y_{pk}(t))$. Denoting the number of particles contained in the k -cloud per unit depth by N_{pk} ($= \bar{N}_{pk}/\bar{n}_{pr}\bar{L}^2$), where n_p is the number density of particles, one obtains a conservation equation of the particles in this cloud:

$$2\pi y_{pk} N_{pk} = 2\pi y_{pk}^* N_{pk}^*$$

or

$$N_{pk} = (y_{pk}^*/y_{pk}) N_{pk}^*, \quad (10)$$

where the asterisk denotes the conditions of particles in the k -cloud at the injected point. A brief illustrative sketch of the cloud in the physical space is given in figure

1. It must be borne in mind that the number density of the particles in each cloud cannot be defined, because the cross-sectional area ΔS_{pk} is not known at time t ($> t^*$). The particle number density n_p in the flow field is, however, defined by space-averaging as will be shown later. In the present analysis, the number density \bar{n}_{pr} at the reference position will be specified as a boundary condition.

In this approximation, the particle phase is considered to be an ensemble of a large number of small clouds. Therefore, we can solve the particle-phase flow by following the behaviour not of all the particles but of all the clouds injected into the flow field. Obviously,

$$\sum 2\pi y_{pk} N_{pk} = N_p, \tag{11}$$

must be satisfied, where the left-hand side is the sum of the number of particles contained in all the clouds and the right-hand side is the total number of particles that are actually present at that time in the flow field.

2.2. Gas phase

In order to evaluate the gas-particle interaction terms, let us define some space-averaged quantities by

$$F_p = \nu_r \left(\frac{1}{S_p} \right) \sum N_{pk} f_{pk}, \tag{12}$$

where f_{pk} denotes a contribution of a representative particle of the k -cloud. Here the summation is taken over the clouds whose centres (x_{pk}, y_{pk}) are in the averaging domain $S_p (= \bar{S}_p / L^2)$. If $f_{pk} = 1$ is substituted into (12), F_p gives the particle density $\rho_p (= \frac{4}{3} \pi \bar{r}_p^3 \bar{\rho}_{mp} \bar{n}_p / \bar{\rho}_r)$ at the centre of the domain S_p , and if the drag force on a particle is used for f_{pk} in this equation, $-F_p$ can be taken as the force exerted on a unit volume of the gas at the centre of S_p .

With the aforementioned approximations for the particle phase, the governing equations for the gas phase are given by

$$\frac{\partial U}{\partial t} + \frac{\partial F}{\partial x} + \frac{\partial G}{\partial y} + H + H_p = 0, \tag{13}$$

where

$$U = \begin{bmatrix} \rho \\ \rho u \\ \rho v \\ e \end{bmatrix}, \quad F = \begin{bmatrix} \rho u \\ \rho u^2 + p/\gamma \\ \rho uv \\ u(e + p/\gamma) \end{bmatrix}, \quad G = \begin{bmatrix} \rho v \\ \rho uv \\ \rho v^2 + p/\gamma \\ v(e + p/\gamma) \end{bmatrix}, \tag{14}$$

$$H = \frac{1}{y} \begin{bmatrix} \rho v \\ \rho uv \\ \rho v^2 \\ v(e + p/\gamma) \end{bmatrix}, \quad H_p = \begin{bmatrix} 0 \\ F_{px} \\ F_{py} \\ W_p \end{bmatrix},$$

$$F_{px} = \nu_r \left(\frac{1}{S_p} \right) \sum N_{pk} A_{pk} (u - u_{pk}),$$

$$F_{py} = \nu_r \left(\frac{1}{S_p} \right) \sum N_{pk} A_{pk} (v - v_{pk}).$$

$$W_p = uF_{px} + vF_{py} - \nu_r \left(\frac{1}{S_p} \right) \sum N_{pk} \left\{ A_{pk} [(u - u_{pk})^2 + (v - v_{pk})^2] - \frac{\theta}{(\gamma - 1)} B_{pk} (T - T_{pk}) \right\}.$$

This system is supplemented by

$$e = \frac{p}{\gamma(\gamma-1)} + \frac{1}{2}\rho(u^2 + v^2), \tag{15}$$

$$p = \rho T, \tag{16}$$

$$c^2 = T. \tag{17}$$

3. Numerical scheme

First we consider the equations for the gas phase interacting with the particle phase. Let $L_x(\Delta t)$ and $L_y(\Delta t)$ designate difference operators yielding solutions to the one-dimensional equations

$$\frac{\partial U}{\partial t} + \frac{\partial F}{\partial x} + H_x + H_{px} = 0, \tag{18a}$$

$$\frac{\partial U}{\partial t} + \frac{\partial G}{\partial y} + H_y + H_{py} = 0, \tag{18b}$$

where

$$H_x = \begin{bmatrix} 0 \\ 0 \\ 0 \\ 0 \end{bmatrix}, \quad H_y = \frac{1}{y} \begin{bmatrix} \rho v \\ \rho uv \\ \rho v^2 \left(e + \frac{p}{\gamma} \right) \\ v \left(e + \frac{p}{\gamma} \right) \end{bmatrix}, \quad H_{px} = \begin{bmatrix} 0 \\ F_{px} \\ 0 \\ W_{px} \end{bmatrix}, \quad H_{py} = \begin{bmatrix} 0 \\ 0 \\ F_{py} \\ W_{py} \end{bmatrix}. \tag{19}$$

Here,

$$\left. \begin{aligned} W_{px} &= uF_{px} - \nu_r \left(\frac{1}{S_p} \right) \sum N_{pk} A_{pk} (u - u_{pk})^2, \\ W_{py} &= vF_{py} - \nu_r \left(\frac{1}{S_p} \right) \sum N_{pk} \left\{ A_{pk} (v - v_{pk})^2 - \frac{\theta}{(\gamma-1)} B_{pk} (T - T_{pk}) \right\}, \end{aligned} \right\} \tag{20}$$

and

$$H = H_x + H_y, \quad H_p = H_{px} + H_{py}, \tag{21}$$

is satisfied

The solution for the gas-phase flow at time $t + \Delta t$ is obtained by successively applying L_x and L_y , to second-order accuracy,

$$U^{n+1} = L_x(\frac{1}{2}\Delta t) L_y(\Delta t) L_x(\frac{1}{2}\Delta t) U^n, \tag{22}$$

where n denotes the time step. In this solution procedure, the particle flow field is fixed to be $U_p^{n+\frac{1}{2}}$, which is the particle-phase solution at time $t + \frac{1}{2}\Delta t$, defined as $\frac{1}{2}(U_p^n + U_p^{n+1})$.

The solution for the particle phase is obtained by applying a simple predictor-corrector algorithm (Zucrow & Hoffman 1977). This procedure is written as follows:

$$U_p^{n+1} = L_{pt}(\Delta t) U_p^n, \tag{23}$$

where L_{pt} denotes the difference operator of (7). In this procedure, the gas-phase flow field is fixed to be $U^{n+\frac{1}{2}}$, which is given by $\frac{1}{2}(U^{n+1} + U^n)$.

First, U_p^1 is obtained from given initial values of U^0 and U_p^0 . Next, the solution for the gas phase U^1 is obtained by applying (22) with U^0 and $U_p^{\frac{1}{2}} = \frac{1}{2}(U_p^0 + U_p^1)$. With

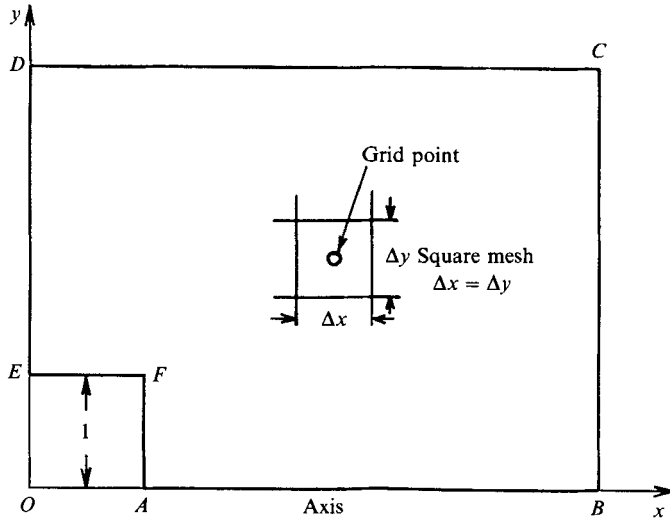


FIGURE 2. Geometry of calculation domain.

$U^{\frac{1}{2}} = \frac{1}{2}(U^0 + U^1)$ and U_p^0, U_p^1 is once again calculated from (23). Finally, U^1 is obtained from (22) with U^0 and a new $U_p^{\frac{1}{2}} = (\frac{1}{2}U_p^0 + U_p^1)$. Thus the unit process is composed of these four steps. The procedure is repeated until the solution U^n as well as U_p^n at a specified time t is obtained. In the present analysis, a piecewise-linear interpolation method (PLM) (Collella & Glaz 1983) is applied to (18) (see the Appendix). Then the time interval Δt is controlled by the Courant–Friedrichs–Lewy condition.

Theoretically, we have two kinds of characteristic (non-dimensional) times for the particle phase, $t_{pV} = 1/A_p$ and $t_{pT} = 1/B_p$. Strictly speaking, the time interval Δt must be controlled by these characteristic times as well as the CFL condition. In the present calculations, it was confirmed that the time intervals Δt determined by the CFL condition were always much smaller than both t_{pV} and t_{pT} . Then in each unit process, the time interval Δt was determined by the CFL condition for the gas-phase flow and also used in the particle-phase solution.

In the numerical analysis, the smallest scale of the flow field ΔL is the mesh size. This suggests that the cross-sectional area ΔS_p of the clouds should be chosen much smaller than the mesh area $(\Delta L)^2$. A time-dependent technique is applied to the present analysis. Then, initial and boundary conditions were specified. From a numerical point of view, the initial conditions are not so important, because the present scheme is robust. The boundary conditions, however, are very critical. As usual, the computational domain is finite, and therefore it is necessary to introduce some numerical boundaries, which will be not physical but artificial ones. The boundary conditions imposed on these numerical boundaries generally affect the numerical results. There are some cases where ill-imposed boundary conditions give unjustifiable or inaccurate results.

In view of this, very careful and extensive numerical experiments have been carried out to check and find the best boundary conditions. We concluded from these numerical experiments that the ‘ambient gas condition’ is the best one that can be applied on the numerical boundaries, at least for the present calculations (Matsuda *et al.* 1987).

Since the cell method is used and the gas variables are defined at the cell centre, as is shown in figure 2, we assume fictitious cells outside the boundaries. The fluxes

Gas (air)	Particles (Al ₂ O ₃)
$\gamma = 1.4$	$\bar{\rho}_{mp} = 4.0 \times 10^3 \text{ kg/m}^3$
$\bar{C}_{pg} = 1005 \text{ J/kg K}$	$\bar{C}_{pp} = 1686 \text{ J/kg K}$
$\bar{\mu} = 1.79 \times 10^{-5} \text{ kg/m s}$ (for $T = 288 \text{ K}$)	
$\delta = 0.5$	
$P_r = 0.75$	

TABLE 1. Physical constants of gas and particles

just on the boundaries are computed by solving the Riemann problem between the state in the fictitious cell and that in the cell just inside the boundary. In these fictitious cells, physical quantities are specified as follows: for the ambient gas condition, we assume that the fictitious cells are filled with an ambient gas in a fixed state.

The computational domain considered here is a cylindrical one, of cross-section as shown in figure 2. The boundaries, on which appropriate boundary conditions are imposed, are the axis AB , the downstream boundary BC , the side CD , the upstream boundary DE , the nozzle or the body wall EF and the nozzle exit plane or the body surface AF . On the boundaries AB and EF , the symmetric condition is applied and on the boundaries BC , CD and DE , the ambient gas condition is given. For jet flows, a uniform sonic jet condition is applied at the nozzle exit plane AF . For a flow around a truncated cylinder, the symmetric condition is applied on the body surface AF .

4. Numerical results

In the present calculations, equal and uniform meshes Δx and Δy were employed. The mesh size is shown on each figure. Physical constants of the gas and the particles used here are listed in table 1.

4.1. One-phase flow

Before proceeding to two-phase flow problems, the corresponding one-phase flows are investigated. These results are compared to the previous experimental and theoretical results, and thereby the reliability of the present scheme is checked. These results will also be compared to the two-phase results to investigate the effects of the presence of particles on the flow field. Schematic views of the flow fields are shown in figure 3. The directions of the jet and ambient gas flows are shown by arrows. In these figures, the subscripts j and ∞ denote the values at the nozzle exit and in the ambient, respectively, and M is the Mach number. The nozzle exit conditions are obtained through an isentropic relationship from the stagnation conditions, which are denoted by the subscript 0. In flows (a) and (b), the reference length L is taken to be the nozzle radius at the exit, and the reservoir conditions are taken as the reference conditions. In flow (c), the length L is taken to be the body radius and the free-stream conditions are taken as the reference conditions.

In the calculations of sonic jets in figure 3(a,b), the whole computational domain was initially filled with the ambient gas and the jet was impulsively exhausted from the nozzle exit at $t = 0$. For the flow around a truncated cylinder in figure 3(c), a supersonic uniform flow impinged on the cylinder at $t = 0$.

Contours of constant density, pressure and Mach number for an underexpanded

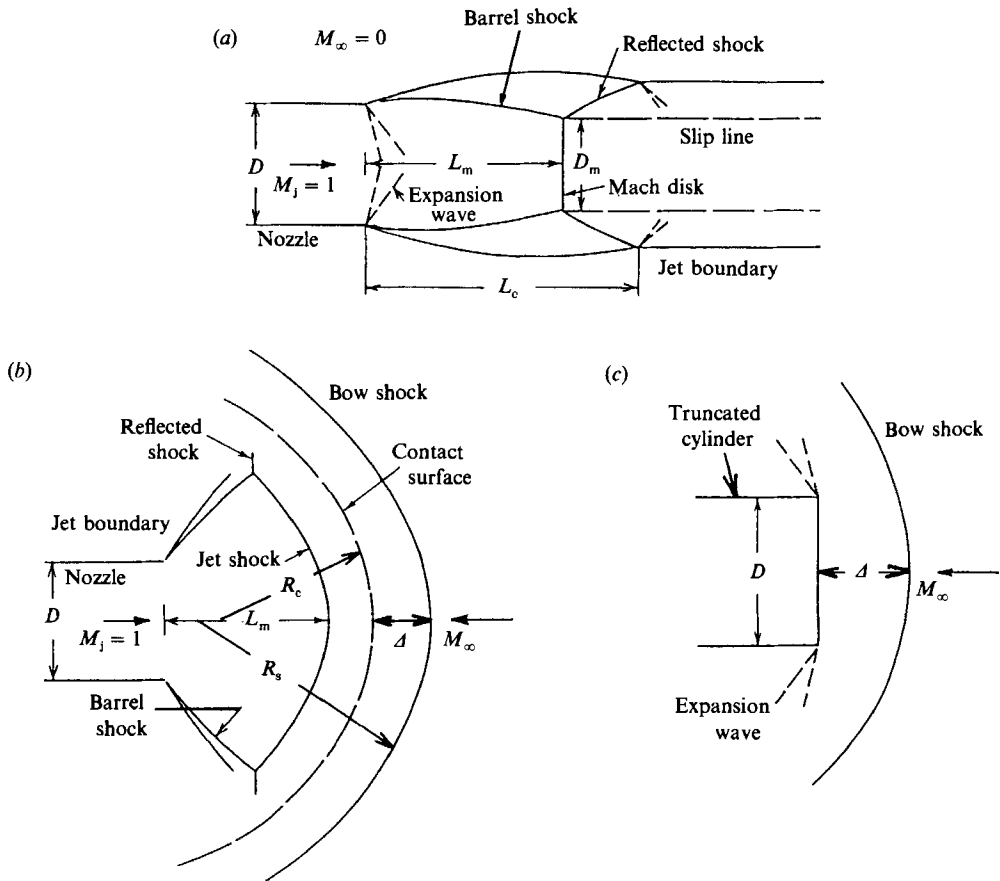


FIGURE 3. Schematic views of flow fields: (a) sonic jet expanded into a stagnant gas; (b) opposing jet; (c) supersonic flow around a truncated cylinder.

free jet are shown in figure 4, where $\bar{p}_0/\bar{p}_\infty = 20$ and F denotes the CFL number. The time history of the density distribution along the symmetric axis is shown in figure 5 for $3000 \leq n \leq 6000$. Here the transient results for $n < 3000$ have been omitted. Figure 5 demonstrates that an almost steady flow field is restricted to only upstream of the Mach disk for large n . In the region downstream of the Mach disk, the density field is slightly fluctuating or oscillatory even for large n . This situation will not always be an unrealistic numerical phenomenon. At a high Reynolds number, the jet boundary is very unstable and then the jet usually experiences a self-sustained oscillation due to a feedback mechanism in connection with the radiation of screech tone (Powell 1953; Umeda, Maeda & Ishii 1987).

In figure 6(a), a schlieren photograph of a uniform sonic jet is shown for the pressure ratio $\bar{p}_0/\bar{p}_\infty = 5.84$. The Reynolds number based on the nozzle diameter is about 10^6 . This photograph was taken with an exposure time of $\frac{1}{60}$ s. The jet appears to be steady and several cell structures can clearly be recognized. Figure 6(b, c) shows shadowgraphs of the jet in figure 6(a). These were taken with an exposure time of $1.1 \mu\text{s}$ and can be considered as instantaneous photographs. We can observe Mach disks, barrel shocks and slip lines on the photographs. An illustrative sketch of the jet in figure 6(c) is shown in figure 6(d). In figure 6(b, c) we can distinguish two types of fluctuations: one very small scale and the other of large scale. The former comes

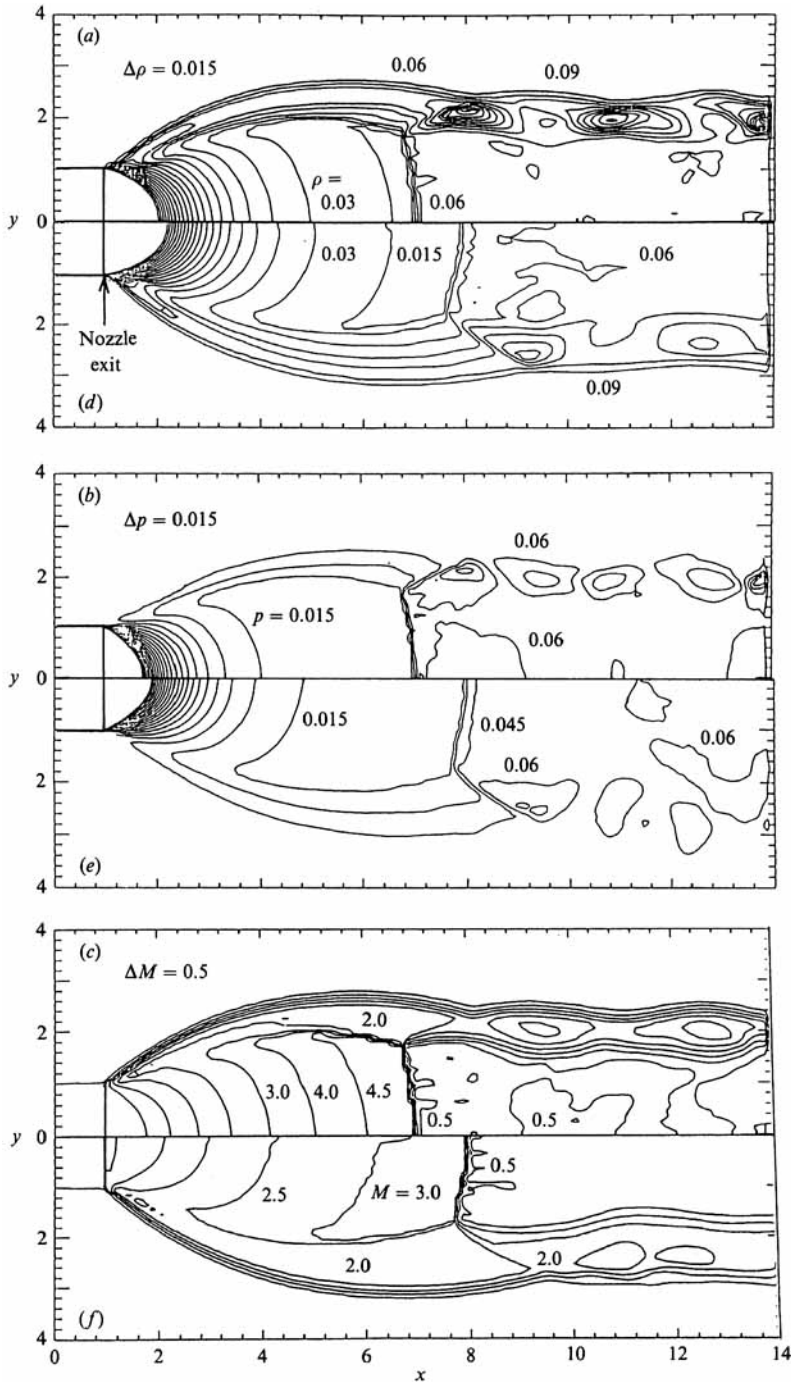


FIGURE 4. Sonic jet expanded into a stagnant gas, $\bar{p}_0/\bar{p}_\infty = 20$, $M_j = 1$, $M_\infty = 0$, $\Delta x = \Delta y = 0.1$. (a, b, c) Constant density, pressure and Mach number contours respectively of dust-free jet, $F = 1.0$, $n = 6000$. (d, e, f) Constant density, pressure and Mach number contours respectively of dusty jet, $\bar{p}_0 = 5$ atm, $T_0 = T_\infty = 290$ K, $L = 5$ cm, $\nu_j = 0.3$, $\bar{r}_p = 1.0$ μm , $K = 50$, $F = 0.8$, $n = 5000(+6000)$.

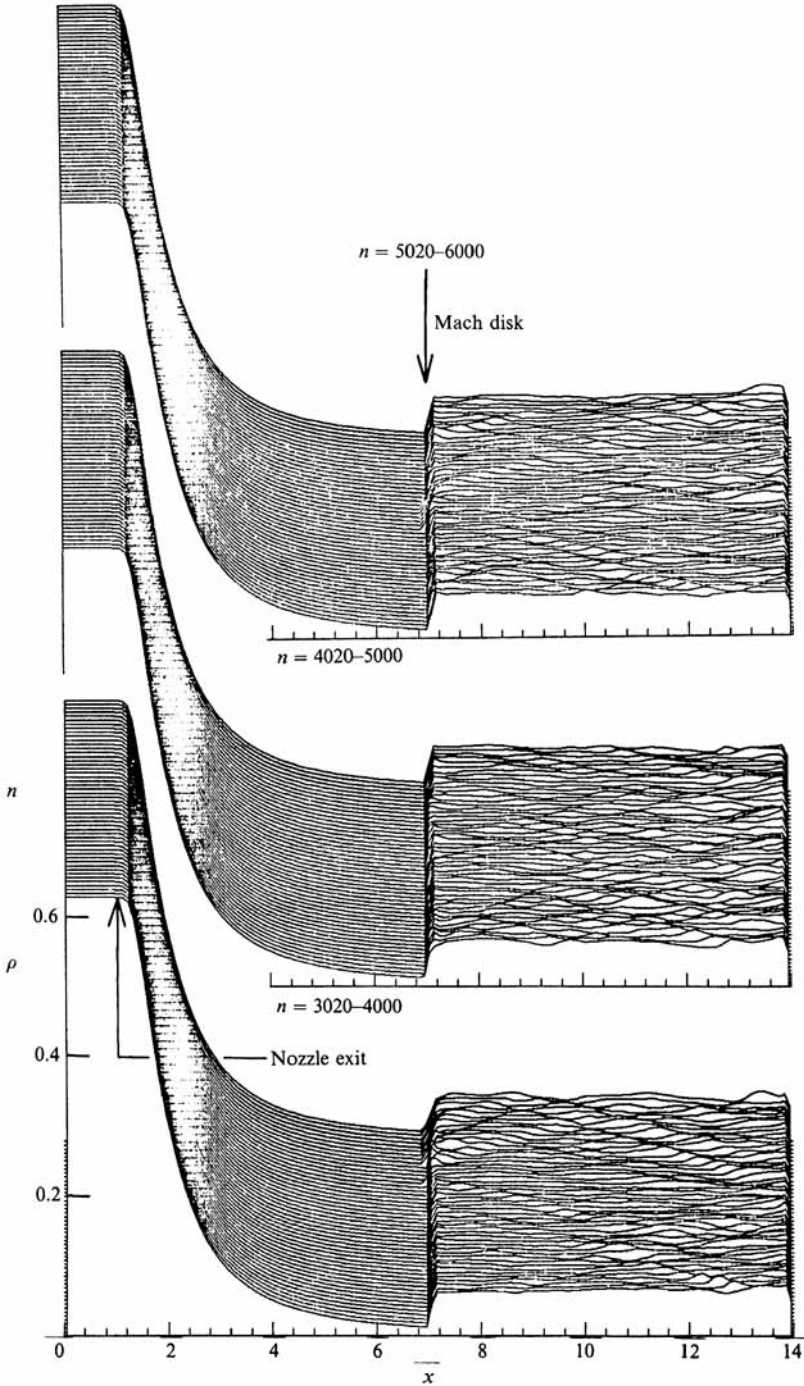


FIGURE 5. Time history of density profile along the jet axis of the dust-free jet shown in figure 4.

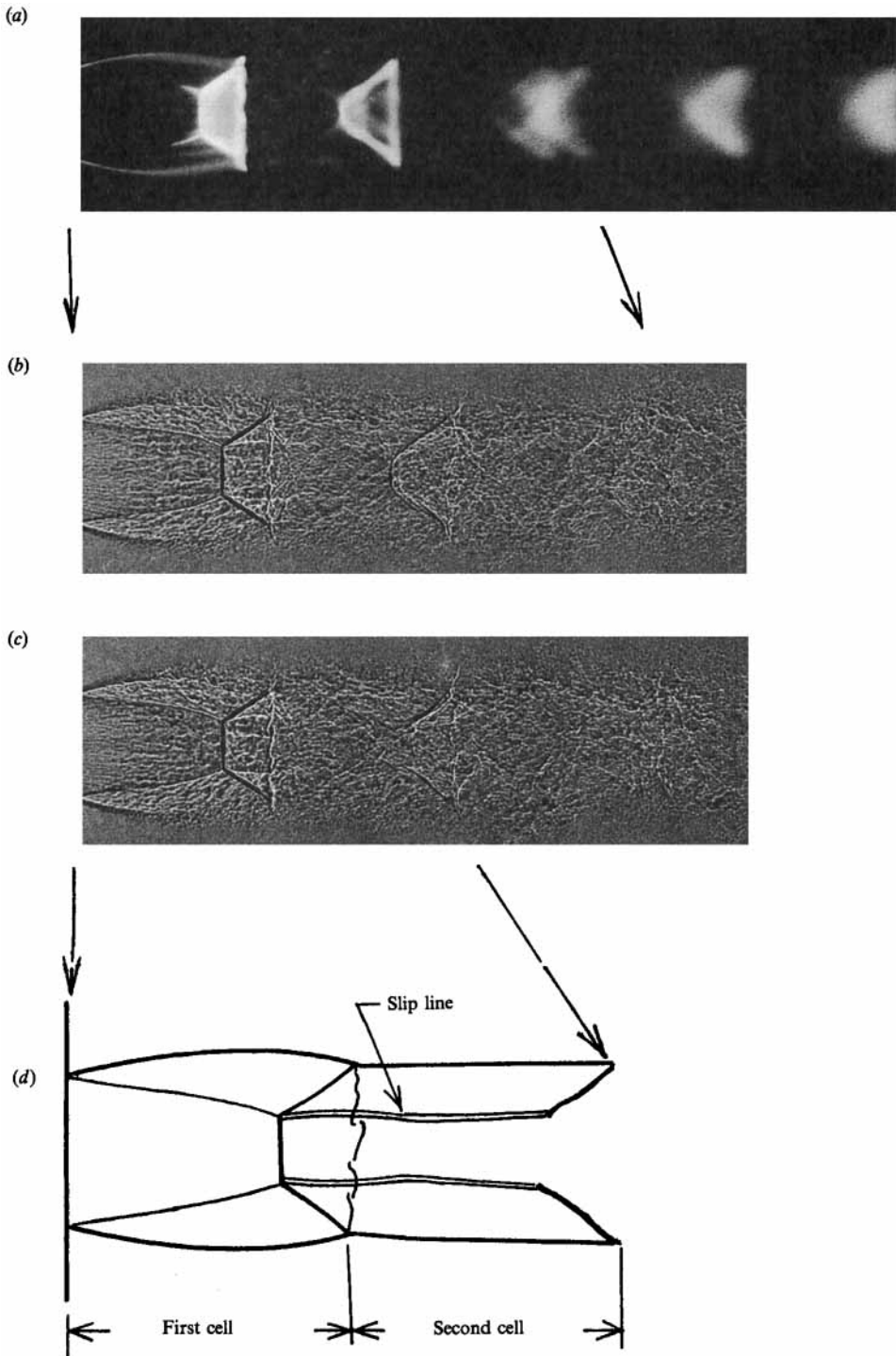


FIGURE 6. Instabilities of dust-free jet for $\bar{p}_0/\bar{p}_\infty = 5.84$.

from the turbulent mixing while the latter may be attributed to the self-sustained oscillation of the jet due to the instabilities of its boundaries and slip lines. The second Mach disk observed in figure 6(b) does not exist in figure 6(c). Obviously, the flow field surrounded by the first Mach disk and the slip lines oscillates with time. Figures 6(b) and 6(c) are only two examples among many instantaneous photographs, taken in our laboratories. These photographs suggest that temporal variation of the shape and size of the second Mach disk and also weak asymmetric modes of oscillation take place in the jet.

Experimentally, it was also confirmed that the asymmetric modes of jet oscillation are dominant in the pressure ratio range of 3 to 4 while symmetric modes tend to become dominant with increasing pressure ratio for $\bar{p}_0/\bar{p}_\infty > 4$. Unfortunately, a pressure ratio of 6 is the highest attainable in our high-pressure wind tunnel. However, using a low-pressure wind tunnel, an experiment for $\bar{p}_0/\bar{p}_\infty = 19.4$ had previously been carried out in our laboratory (Kobayashi, Nakagawa & Nishida 1984) and a comparison with the present result is contained in figure 7. Agreement between them is fairly satisfactory. However, in the low-pressure (density) experiment, it was impossible to take the instantaneous photographs by usual optical methods, and so the detailed characteristics of the jet oscillation remain unknown for $\bar{p}_0/\bar{p}_\infty = 20$ at least for the present.

In spite of this, the present and the previous experiments strongly suggest that the oscillatory character of the flow field is ubiquitous in free jets and the numerical result has simulated this phenomenon. However, as shown in figure 5, the flow field upstream of the Mach disk is relatively stable and the characteristics of the first shock cell are unchanged with time. This situation is also quite consistent with the experiments.

Another important point is that the effects of turbulent mixing on the (first few) shock-cell structures and then on the jet oscillation are not important (Romeo & Sterrett 1963; Powell 1953). An analysis using the Euler equation will, therefore, be appropriate for the present study.

Although it is important to compare the jet oscillation with previous experimental and theoretical results in more detail, there are no available experimental data nor theoretical results for free jets at high pressure ratios. From a theoretical point of view, the jet flow field at a high pressure ratio is highly nonlinear, which prevents us from applying the previous linear analyses to the present study (Tam 1972).

The most important feature of free-jet flow for a very large pressure ratio is that the flow region downstream of the Mach disk is divided into two subregions by the strong slip lines: one is the core region, where the flow is slightly periodic, and the other is the outer region surrounded by the jet boundary and the slip line, where the flow is spatially highly periodic, perhaps because the pressure waves in the outer region are effectively reflected by the jet boundary and the slip line (see figure 4a-c).

The location and the width of the Mach disk and the first shock-cell length obtained in the present calculations are compared with the experiments of Love *et al.* (1959) in figure 7(a). There is excellent agreement between the present and the experimental results.

Contours of constant density, pressure and Mach number for an opposing jet are shown in figure 8 for $\bar{p}_0/\bar{p}_\infty = 20$ and $M_\infty = 2$. The time history of the density profile along the jet axis for the opposing jet is shown in figure 9 which demonstrates a similar behaviour to that in figure 5. However, the flow behaviour in the region downstream of the Mach disk is very different. The locations of the Mach disk, the

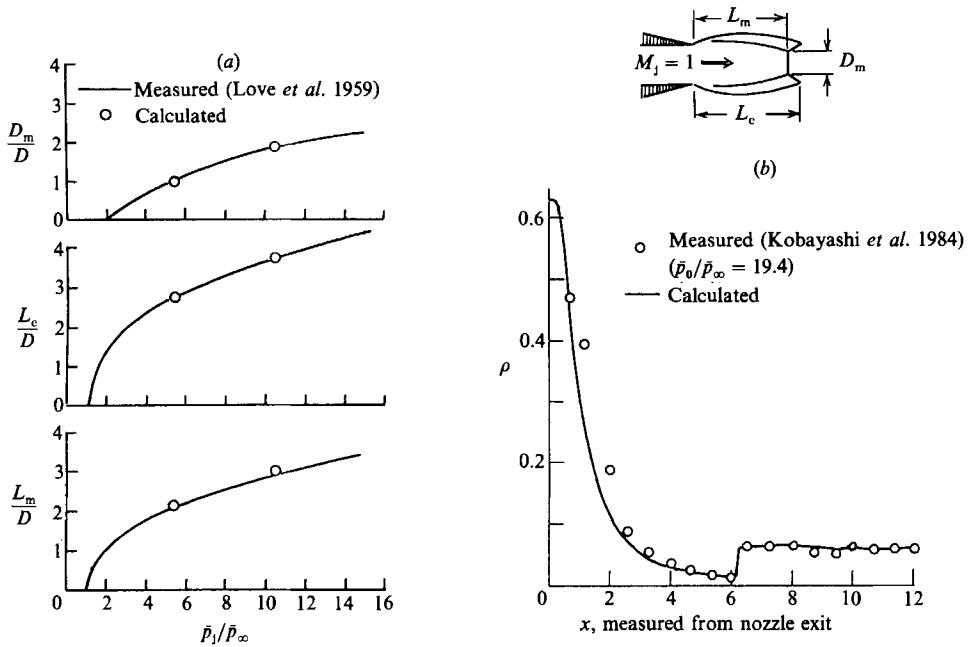


FIGURE 7. Comparison between the present dust-free results and experiments: (a) characteristics of the first shock-cell; (b) density distribution along the jet axis.

contact surface and the bow shock are relatively very oscillatory with time compared to those in the free jet even for large n .

Previous experiments have shown that a very strong and large instability can occur in some situations for an opposing jet (Romeo & Sterrett 1963). In such a case, the pressure fluctuation in an almost dead-air region surrounding the jet boundary near the nozzle exit plays an important role. The pressure variation with time sometimes results in a change of shock-cell pattern or the basic flow structure of the jet. This change in turn produces a large scale of displacement of the free-stream bow shock.

For the flow conditions considered here, however, the present jet is categorized as a very steady one on the opposing jets (Finley 1966). Denoting the Pitot pressure of the free stream by $\bar{p}'_{\infty 0}$, the position of the jet shock L_m divided by the nozzle diameter $D (= 2)$ can be correlated as a function of $\bar{p}_0/\bar{p}'_{\infty 0}$ for all free-stream Mach numbers M_∞ . In figure 10, the numerical results for L_m/D are compared with the experiments of Romeo & Sterrett (1965). Since the present results are oscillatory with time, the data for the position of the jet shock show some scatter. In spite of this, agreement between the numerical and the experimental results is very good.

In the present results, although the contact surface fluctuates with time rather strongly, the bow shock does not appreciably change its shape and size. It experiences only parallel displacement along the jet axis. Then a time-averaged radius of the contact surface R_c was determined from the radius of the bow shock R_s through the approximation $R_s \approx R_c(1 + \Delta/R_c)$, where Δ is a shock stand-off distance for a supersonic flow around a solid sphere with radius R_c . Experimental results for Δ/R_c (Van Dyke 1958) were used to determine R_c in conjunction with the numerical results for R_s . These are plotted in figure 10 (b) against $\bar{p}_0/\bar{p}'_{\infty 0}$. The present results are

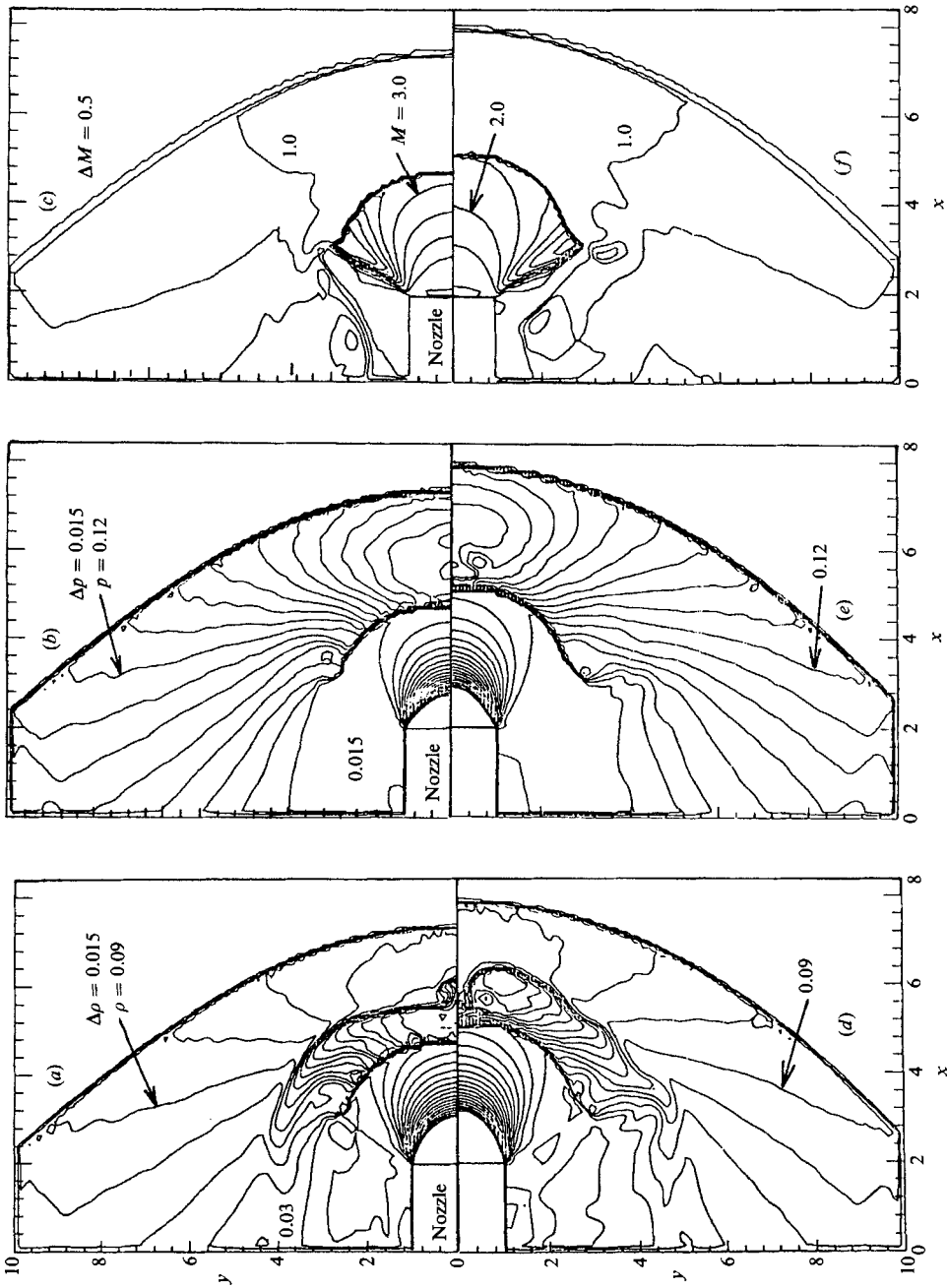


FIGURE 8. Opposing jet, $\bar{p}_0/\bar{p}_\infty = 20$, $M_j = 1$, $M_\infty = 2$, $\Delta x = \Delta y = 0.1$. (a, b, c) Constant density, pressure and Mach number contours respectively of dust-free jet, $F = 1.0$, $n = 9000$. (d, e, f) Constant density, pressure and Mach number contours respectively of dusty jet, $\bar{p}_0 = 5$ atm, $T_0 = T_\infty = 290$ K, $L = 5$ cm, $v_1 = 0.3$, $\tau_0 = 1 \mu\text{m}$, $K = 50$, $F = 0.8$, $n = 5000(+9000)$.

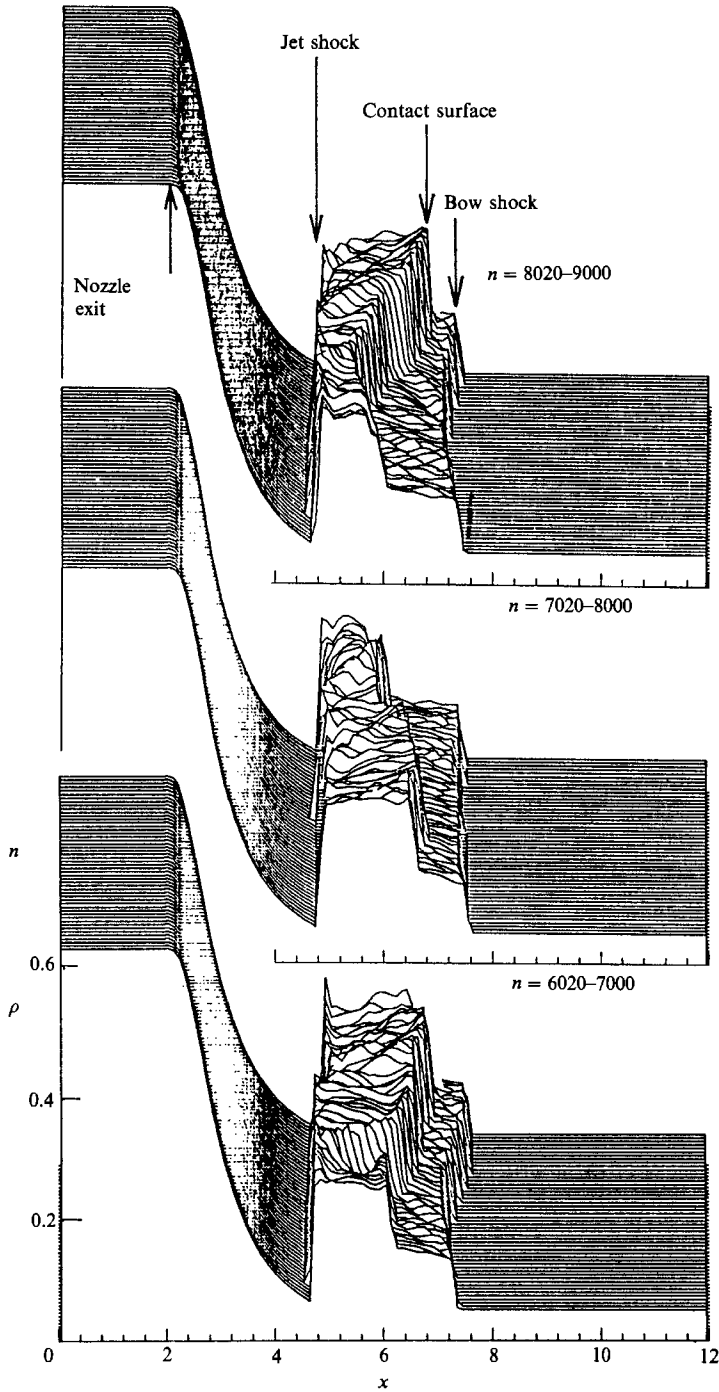


FIGURE 9. Time history of density profile along the jet axis of the dust-free opposing jet shown in figure 8.

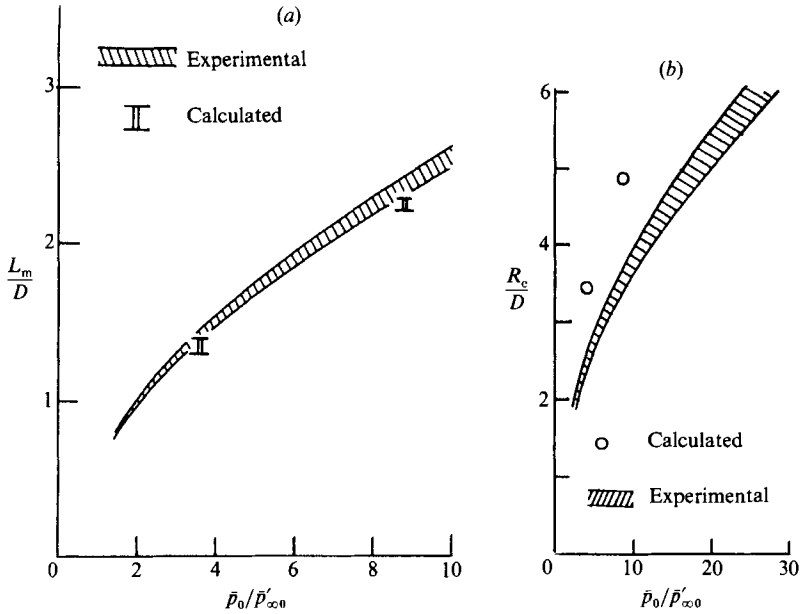


FIGURE 10. Comparison between the present results and experiments for the dust-free opposing jet shown in figure 8: (a) Jet-shock position; (b) time-averaged radius of contact surface.

few tens percent larger than the experiments. This might come from the fact the present Mach number $M_\infty = 2$ is not large enough to use the approximation $R_s \approx R_c + \Delta$ and also to expect a sufficient correlation between R_c and the pressure ratio $\bar{p}_0/\bar{p}'_{\infty 0}$.

Experimentally, it has been observed that the round opposing jet is very sensitive to transverse fluctuations (Romeo & Sterrett 1963). In figure 8(a), one can see a protrusion of the contact surface near the jet axis. The shape and the size of this protrusion change with time. This phenomenon can be attributed to the Rayleigh–Taylor and/or Kelvin–Helmholtz instabilities (stagnation instability). Numerically, the axisymmetric condition is responsible for this large instability. Although the instability of the contact surface was clearly observed even in very stable opposing jets, such a large instability of the contact surface has not been confirmed experimentally. This might be explained by the aforementioned experimental observation that the opposing jet is very sensitive to transverse fluctuations. Hence, it could be said that the axially symmetric calculation may not simulate well some instabilities in the opposing jet. However, it must be emphasized that the instability of the contact surface, for example, in an astrophysical jet (Norman *et al.* 1982), is very sensitive to the density ratio $\bar{\rho}_1/\bar{\rho}_\infty$, and so the present result should be compared with experiment for both the same density and pressure ratios. At least qualitatively, the present numerical results are quite consistent with those of Norman *et al.* (1982) and those of Kössel & Müller (1988).

Contours of constant density, pressure and Mach number for a supersonic flow around a truncated cylinder are shown in figure 11. The space–time diagram of the density distribution along the axis is shown in figure 12(a). This clearly demonstrates a time-convergence of the flow field. At first, the shock wave impinging on the cylinder surface is reflected and the reflected wave propagates upstream. This shock wave travels some distance very fast and then experiences rapid deceleration to form

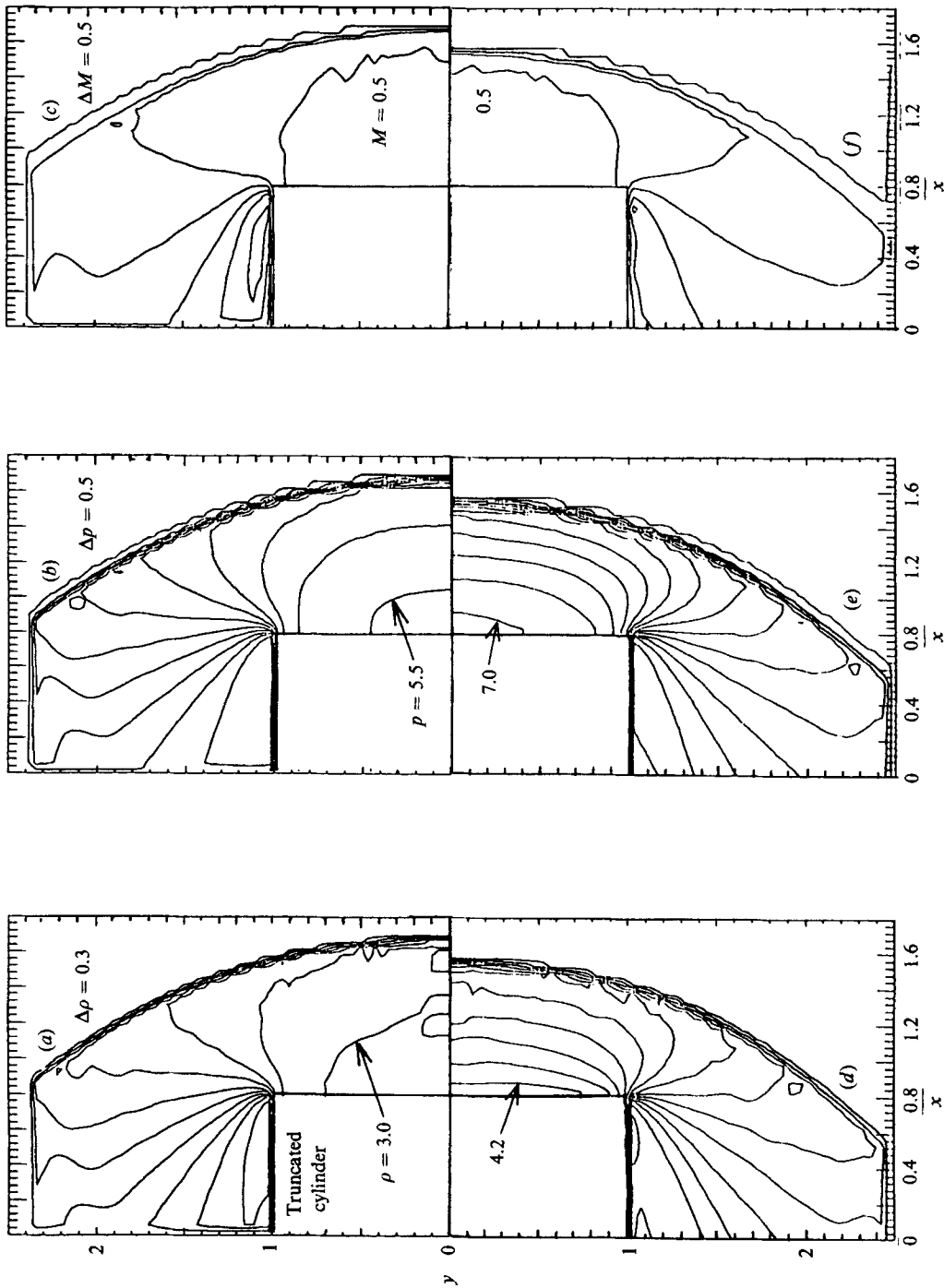


FIGURE 11. Supersonic flow around a truncated cylinder, $M_\infty = 2$, $\Delta x = \Delta y = 0.05$. (a, b, c) Constant density, pressure and Mach number contours respectively of dust-free flow, $F = 1$, $n = 6000$. (d, e, f) Constant density, pressure and Mach number contours respectively of dusty flow, $T_\infty = 290$ K, $L = 5$ cm, $\nu_\infty = 0.3$, $\bar{\nu}_p = 2.0$ μm , $K = 250$, $F = 0.8$, $n = 4000$ (+4000).

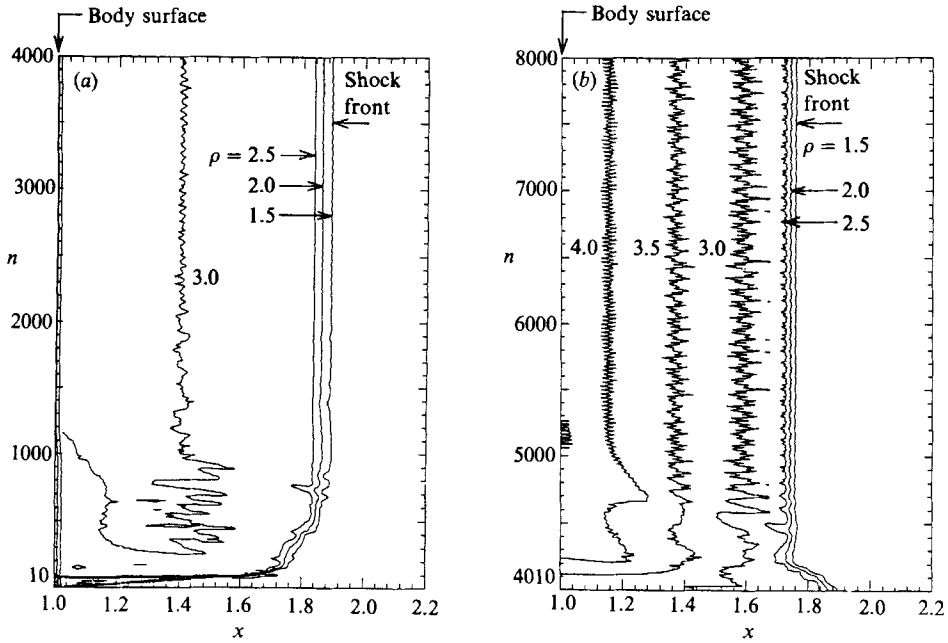


FIGURE 12. Space-time diagram of density distribution along the axis of the supersonic flow around a truncated cylinder, $M_\infty = 2.0$, $\Delta x = \Delta y = 0.05$. (a) Dust-free for $1 \leq n \leq 4000$, $F = 1.0$; (b) dusty for $4001 \leq n \leq 8000$, $\bar{p}_\infty = 0.5$ atm, $T_\infty = 290$ K, $L = 5$ cm, $\bar{r}_p = 2 \mu\text{m}$, $\nu_\infty = 0.3$, $K = 250$, $F = 0.8$.

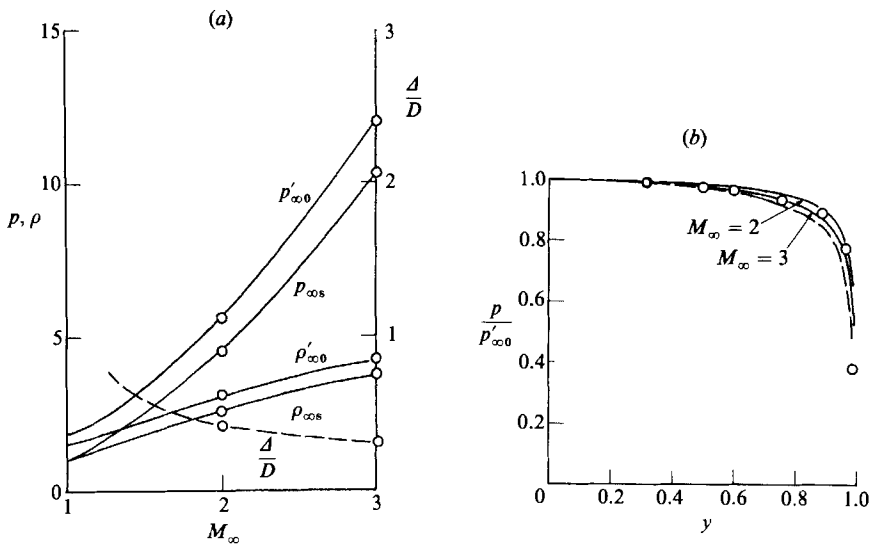


FIGURE 13. Comparison of the present dust-free results with experiments and theories. (a) Shock and stagnation conditions: —, analytical (exact) solutions; ----, experiments (Kendall 1959), \circ , present results. (b) Pressure distribution along the body surface: \circ , $M_\infty = 4.76$ (Kendall 1959); ----, $M_\infty \geq 3$ (Chuskin 1962); —, present results.

a stationary bow shock. The rapid deceleration in turn produces pressure waves which propagate downstream. The high-temperature gas that was produced by the first reflection of the incident shock remains for a very long time in front of the body surface. The final steady state is obtained after this hot gas cloud has been completely removed from the flow field.

In figure 13, the numerical results are compared with experiments and theories (Kendall 1959; Chuskin 1962). Here Δ is the shock stand-off distance, $p_{\infty s}$ and $\rho_{\infty s}$ are the pressure and the density of the gas just behind the bow shock on the axis, and $p'_{\infty 0}$ and $\rho'_{\infty 0}$ are the pressure and the density at the stagnation point on the body surface, respectively. Exact values of these quantities were obtained analytically. Profiles of the pressure distributions along the body surface are shown in figure 13(b), showing excellent agreement between the present results and the experimental and theoretical ones.

4.2. Particle behaviour in a gas flow

Practically and theoretically, it is important to investigate the motion of particles in gas flows (Healy 1970; Michael & Norey 1969; Morsi & Alexander 1969; Probst & Fassio 1970). In this section, we investigate the behaviour of particles in the flows obtained in the previous section. In the jet flows, the particles are injected into the gas jet at fixed points on the nozzle exit plane at each time step after the final step in the one-phase solutions (see figures 4 and 8). In the flow around a truncated cylinder, the particles are injected into the flow field in a similar manner on a plane perpendicular to the symmetric axis ahead of the bow shock. In every case, the particles are assumed to have the same velocities and temperatures as those of the gas at the injected positions.

Since the gas flows are not steady, the gas and the particle flows are solved simultaneously even in the limiting case where $\nu \rightarrow 0$. Only the flow around a truncated cylinder is steady for large n and then the particle motion is solved for a fixed flow field of the gas.

Streaklines of the particles in a sonic jet expanded into a stagnant ambient gas are shown in figure 14 for the particle radii $\bar{r}_p = 1.0, 2.0$ and $5.0 \mu\text{m}$, respectively, where arrows denote the velocity vectors of the particles. The particles are injected at points $y_{pk}^* = 0.1(k-0.5)$ ($k = 1-10$) on the nozzle exit plane. For $\bar{r}_p = 1.0 \mu\text{m}$, all the particles flow through the gas inside the jet boundary. As shown in figure 4, the gas flow field is divided into several subregions by the jet boundary, shock waves and slip lines. The flow behind the Mach disk and surrounded by the strong slip lines is subsonic, so a subsonic 'inverse' jet is submerged in the faster annular supersonic jet. In this region, the gas flow fluctuates and the small particles ($\bar{r}_p = 1.0 \mu\text{m}$) follow the fluctuation. The fluctuation of the particle motion becomes smaller for the larger particles ($\bar{r}_p = 2.0$ and $5.0 \mu\text{m}$). It is interesting that an appreciable concentration of particles occurs near the gas jet boundary for $\bar{r}_p = 1.0 \mu\text{m}$. The particles along the outer streaklines penetrate through the gas jet boundary into the ambient region for $\bar{r}_p = 2.0$ and $5.0 \mu\text{m}$. The maximum width of the dusty region becomes larger with increasing radius. Theoretically, however, for fixed gas jet conditions, the width of the dusty region will decrease again for sufficiently large particles. Then the spreading region of the particles becomes maximum at a certain size of particle.

In order to investigate the particle behaviour more systematically, it is convenient to introduce non-dimensional parameters such as Γ_τ , Γ_ρ and R_e , where R_e is the Reynolds number of the gas-phase flow (Chung & Troutt 1988). Although this Reynolds number is not primarily important for the particle-phase flow, it is important to justify the use of the Euler equations for the gas-phase flow. In the

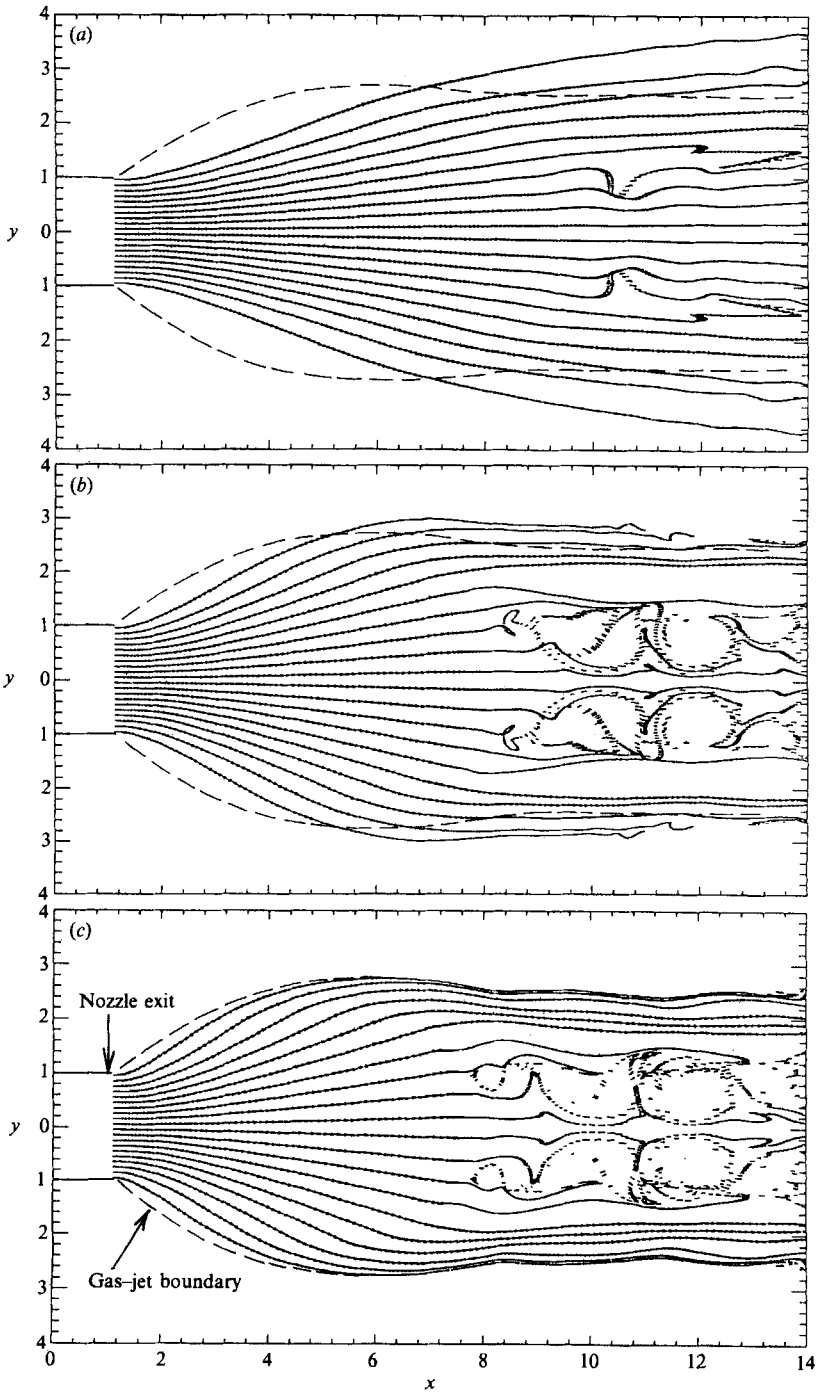


FIGURE 14. Velocity vectors of particles along streaklines in a jet expanded into a stagnant gas, $\bar{p}_0 = 5$ atm, $\bar{p}_0/\bar{p}_\infty = 20$, $T_0 = T_\infty = 290$ K, $M_j = 1$, $M_\infty = 0$, $L = 5$ cm, $\Delta x = \Delta y = 0.1$, $F = 0.8$, $n = 1000(+6000)$. The scaling length for Ψ is the nozzle diameter $2L$. (a) $\bar{r}_p = 5.0$ μm , $\Psi = 4.8$; (b) $\bar{r}_p = 2.0$ μm , $\Psi = 0.69$; (c) $\bar{r}_p = 1.0$ μm , $\Psi = 0.17$.

present study, R_e is of $O(10^6)$ based on the nozzle diameter, which justifies the use of the Euler equations for the gas-phase analysis.

The particle behaviour in a gas flow can be characterized by the Stokes number Ψ defined by $[\bar{\rho}_{mp}(2\bar{r}_p)^2/18\bar{\mu}_j f_{pj}]/(\bar{L}/\bar{U})$, where \bar{U} is an appropriate reference velocity. For a sonic jet, this can be rescaled without loss of generality as

$$\Psi = \frac{\bar{\rho}_{mp}(2\bar{r}_p)^2 \bar{U}_j}{18 \bar{\mu}_j f_{pj} 2\bar{L}}, \quad (24)$$

where $2\bar{L}$ is the nozzle diameter. Since $\bar{U}_j = \bar{c}_j$ and $f_{pj} = 1$ in the present analysis, we have

$$\Psi = \frac{1}{2} \Gamma_\tau = \frac{1}{2A_{pj}}. \quad (25)$$

This was used to investigate the particle dispersion in incompressible subsonic jets by Chung & Troutt (1988). In their analysis, the nozzle diameter $\bar{D} = 2\bar{L}$ is taken as the scaling length characterizing the large turbulent structures. In the present study, we can take the nozzle diameter as the scaling length of the shock-cell structure. By doing so, we shall be able to expect some qualitative and quantitative analogies between the present results and those obtained by them.

For $\Psi \gg 1$, the particles will not have sufficient time to respond to the gas flow and will move in a nearly rectilinear path. In this case the flow spreading rate will be larger than the lateral dispersion rate of the particles. For $\Psi \ll 1$, the particles have sufficient time to respond to the spreading velocity field of the gas jet and should disperse laterally with the spreading rate of the gas jet. On the other hand, for $\Psi = O(1)$ the gas jet will be able to capture the particles and fling them beyond the gas jet boundary. In figure 14, the value of this parameter is shown in each case. The present results are clearly quite consistent with the previous discussion.

In an underexpanded free jet, shock-cell structures appear and the gas experiences very rapid and strong expansions and compressions in the jet. In such a case, the modifying factor f_p will deviate significantly from unity. Then the parameter Ψ defined by (25) may be applicable with acceptable validity only in the analysis of particle behaviour in the region upstream of the Mach disk.

Particle streaklines in an opposing jet are shown in figure 15 for $\bar{r}_p = 1.0, 2.0$ and $5.0 \mu\text{m}$. All sizes of particles flow through interfacial region between the jet gas and the mainstream gas, at least under the present flow conditions. We can see that the particles are accelerated very smoothly in the expansion region of the jet. After the particles pass through the jet shock, they are decelerated by the compressed gas and also fluctuate significantly owing to the gas flow fluctuations near the contact surface.

For small particles ($\bar{r}_p = 1.0$ and $2.0 \mu\text{m}$), embedded particle-free regions appear as shown in figure 15. Moreover, we can find some interesting characteristics of the particle flow. The particles that enter the flow region between the jet shock and the contact surface are decelerated and then convected by the gas into the radial direction. Finally, they are pushed back in the mainstream direction opposite to the jet exhaust direction. Since the particle has much larger inertia than the gas molecule, it cannot completely follow the gas motion. The particle clouds, therefore, form a cocoon with some thickness which depends on the jet and the particle conditions. In the present calculations, this thickness of the cocoon wall becomes minimum for about $\bar{r}_p = 2.0 \mu\text{m}$. The outer radius of this cocoon becomes larger with increasing particle size and its structure depends on the particle radius. When the

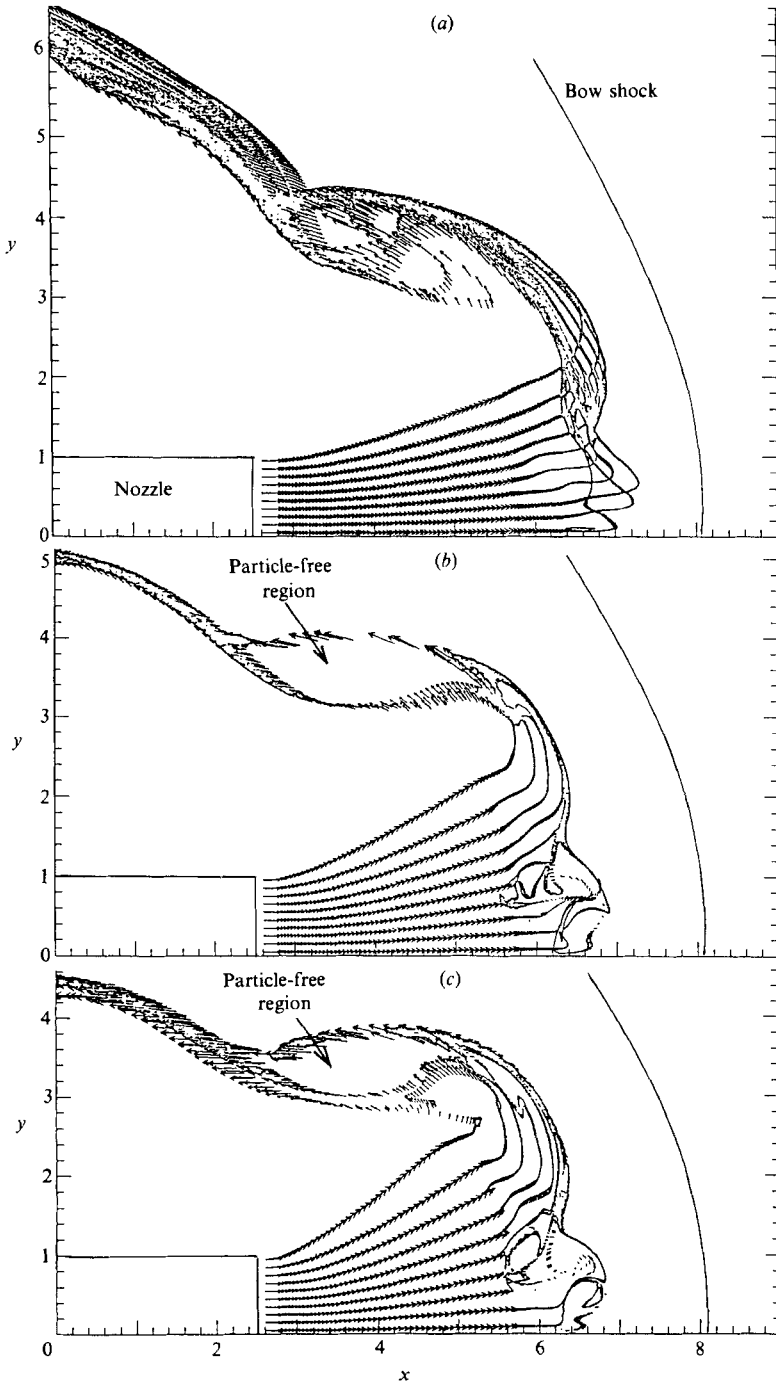


FIGURE 15. Velocity vectors of particles along streaklines in an opposing jet, $\bar{p}_0 = 5$ atm, $\bar{p}_0/\bar{p}_\infty = 20$, $T_0 = T_\infty = 290$ K, $M_1 = 1$, $M_\infty = 2$, $L = 5$ cm, $\Delta x = \Delta y = 0.1$, $F = 1$, $n = 1500(+9000)$. The scaling length for Ψ is the nozzle diameter $2\bar{L}$. (a) $\bar{r}_p = 5.0$ μm , $\Psi = 4.8$; (b) $\bar{r}_p = 2.0$ μm , $\Psi = 0.69$; (c) $\bar{r}_p = 1.0$ μm , $\Psi = 0.17$.

particle size is large ($\bar{r}_p = 5.0 \mu\text{m}$), the particles injected at points near the jet axis flow along the inner wall and those injected near the outer edge of the nozzle flow along the outer wall of the cocoon. This situation is reversed for particles with radius $\bar{r}_p = 1.0 \mu\text{m}$. The result for $\bar{r}_p = 2.0 \mu\text{m}$ is intermediate between the above two.

Particle trajectories depend significantly on the flow structure and fluctuations of the gas-phase flow. When the particles enter the fluctuating flow region of the gas, at first their velocities begin to follow the fluctuations relatively very slowly owing to their large inertia. Once their motions are perturbed, however, they travel through the gas flow field almost independently of each other, because the particle pressure is not present. Then the trajectories of two particle clouds, which were at first adjacent, can deviate appreciably during their travel through the gas flow field. This situation is appreciably enhanced if these two particle clouds enter different parts of the flow region.

It will be very difficult to characterize the particle behaviour by one parameter such as Ψ defined previously, because every particle flows through at least several different parts of the flow field. For example, the values of this parameter described in figure 15 do not seem to give us any useful information about the particle cocooning. The thickness of the particle cocoon wall becomes minimum for $\Psi = O(1)$. It is, however, not clear that this result is generally valid and the particle cocooning can be correlated with this parameter. More extensive numerical calculations will be necessary to clarify the existence of correlation of the particle cocooning with Ψ .

The particle streaklines in the gas flow around a truncated cylinder are shown in figure 16. It is assumed that the particles that impinge on the body surface are reflected perfectly elastically. As was discussed previously, the gas flow becomes substantially steady for large time step n . The streaklines shown in this figure can, therefore, be taken as the streamlines of the particles.

The particles that pass through the bow shock are decelerated by the gas in the shock layer. In general, however, particles whose sizes are larger than some critical size cannot be decelerated completely in the shock layer and then impinge on the body surface with a finite velocity.

In practical situations, the particles that impinge on the body surface will be reflected with finite velocities. The change in the mechanical and thermal properties of the impinged particles due to the collision with the body surface will depend on the physical conditions of the particles and the surface and also will depend on the velocities of the impinged particles. For simplicity, however, in the present analysis, only two extreme cases will be considered: perfectly elastic reflection and perfectly inelastic reflection. Furthermore, in the former case, it is assumed that only the velocity component normal to the body surface is reversed and the tangential component is unchanged (specular reflection). In the latter case, it is also assumed that the impinged particles stick to or are absorbed by the body surface and the shape and size of the body are not affected by the impinged particles.

For $\nu \rightarrow 0$, the gas flow is not affected by the presence of particles. Then the particle streamlines in the case of a perfectly inelastic reflection are the same as of a perfectly elastic reflection except for the streamlines of the reflected particles.

As shown in figure 16, the particle streamlines in the shock layer strongly depend on the particle size. For $\bar{r}_p = 0.5 \mu\text{m}$ and $1.0 \mu\text{m}$, the particles impinging on the body surface have very small velocity components normal to the body surface. Then the effect of the particle reflection is very small. It is important to point out that a very large concentration of particles appears near the shoulder of the body surface. With increasing particle size, the particles impinge on the body surface with larger normal

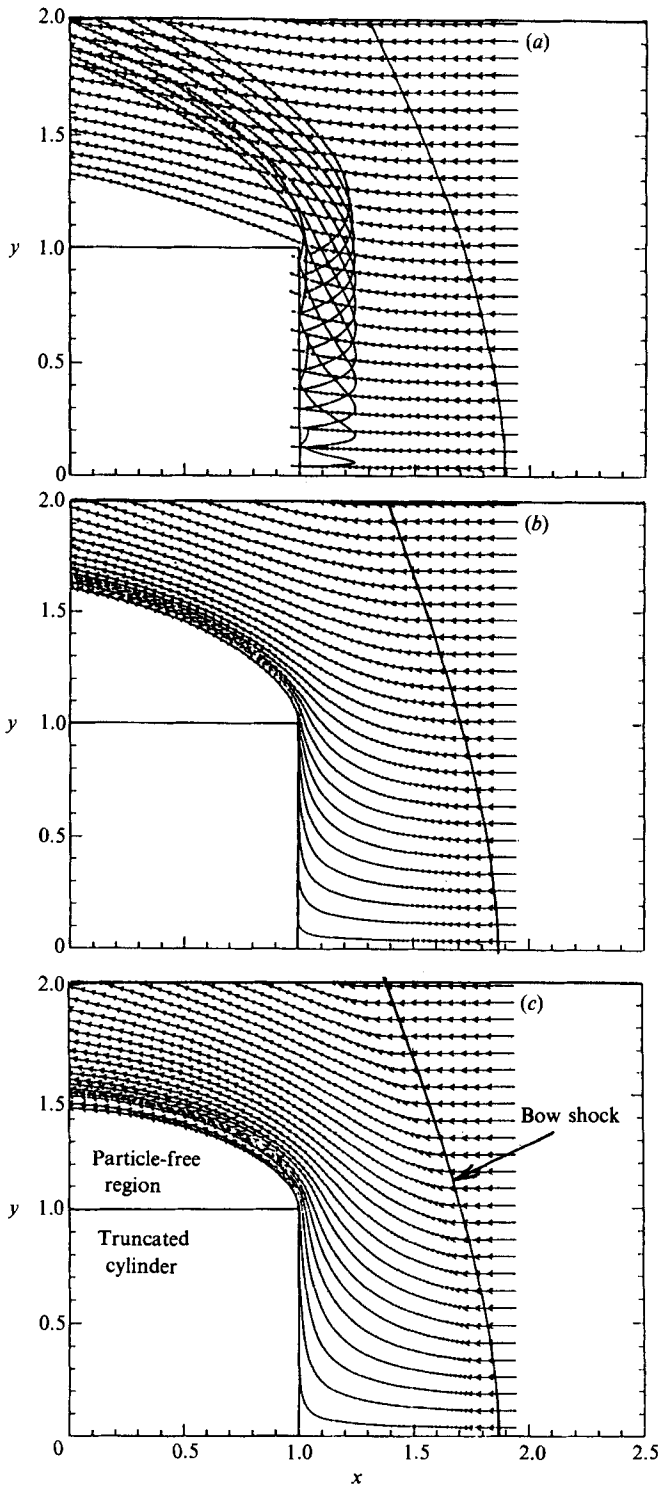


FIGURE 16. Velocity vectors of particles along streamlines in a supersonic flow around a truncated cylinder, $\bar{p}_\infty = 0.1$ atm, $M_\infty = 2$, $T_\infty = 290$ K, $\bar{L} = 5$ cm, $\Delta x = \Delta y = 0.02$. The scaling length for Ψ is the shock stand-off distance $\bar{\Delta}$. (a) $\bar{r}_p = 2.0$ μm , $\Psi = 1.2$; (b) $\bar{r}_p = 1.0$ μm , $\Psi = 0.51$; (c) $\bar{r}_p = 0.5$ μm , $\Psi = 0.17$.

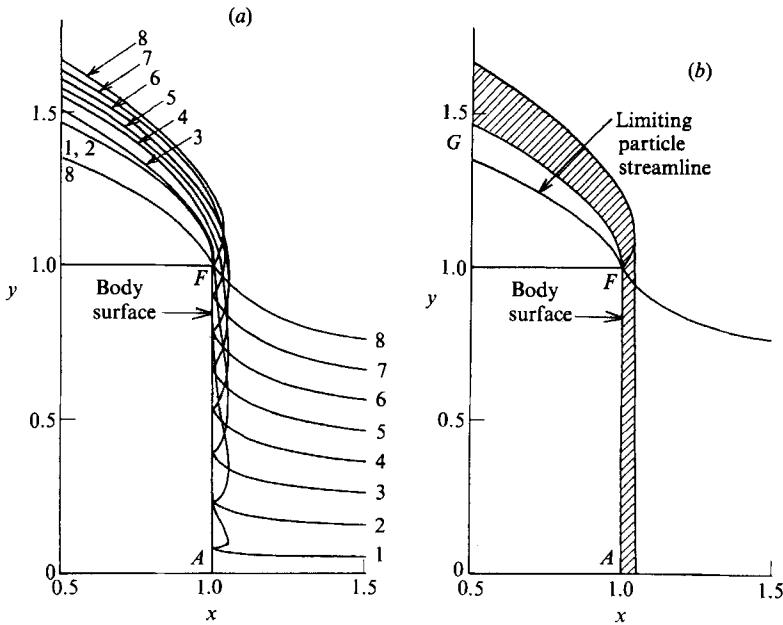


FIGURE 17. Streamlines of particles impinging on the body surface, $\bar{p}_\infty = 0.5$ atm, $M_\infty = 2$, $\bar{T}_\infty = 290$ K, $\bar{L} = 5$ cm, $\bar{r}_p = 2$ μ m, $\Delta x = \Delta y = 0.02$, $\Psi = 0.59$. (a) Particle streamlines for completely elastic reflection from the body surface. (b) Intersecting region of particle streamlines.

velocity components, and then the reflected particles travel upstream larger distances until they are decelerated by the gas flow and are again pushed back in the main flow direction. It is interesting that the particles impinging on the surface near the body axis experience a few collisions with the body surface, before they flow out of the shock layer in front of the body. The number of collisions that a particle experiences depends on the particle size and the first impinging location of the particle.

In every case, the particle-free region appears in the flow region between the outer side of the cylinder and the limiting particle streamline. At least theoretically, the extent of this region will become infinitely small in two limiting cases, where $\bar{r}_p \rightarrow 0$ and $\bar{r}_p \rightarrow \infty$. In the former, the particles will follow the gas flow almost completely, and in the latter, they are not affected by the gas flow appreciably. In a certain intermediate case, the extent of the particle-free region becomes maximum under the fixed gas conditions and body size.

For more detailed investigation of the particle streamlines in the case of the perfectly elastic reflection, streamlines of the particles that impinge on the body surface are shown in figure 17(a) for $\bar{p}_\infty = 0.5$ atm, $M_\infty = 2.0$ and $\bar{r}_p = 2.0$ μ m. Obviously these particles flow along very complicated streamlines. On the line AFG in figure 17(b), the particle concentration becomes infinitely large, and then the line FG would form a particle sheet in the flow field, if the loading ratio is not zero but finite. The hatched region in figure 17(b) is the region where the intersections of the particle streamlines occur.

It is important practically to investigate the collection factor E_p of a body suspended in a gas stream. This is defined as the square of ratio of the radial distance of the outermost streamline of particles in the uniform flow region that can impinge

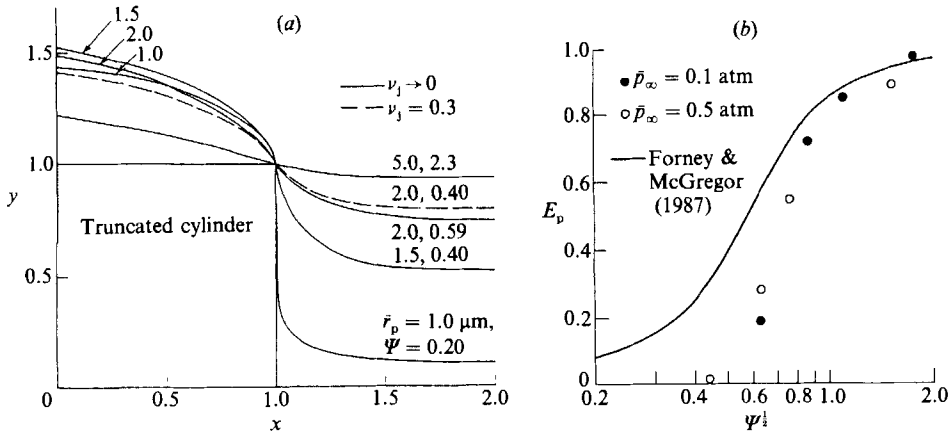


FIGURE 18. Limiting particle streamline and collection factor. (a) Limiting particle streamlines in a supersonic flow around a truncated cylinder, $\bar{p}_\infty = 0.5$ atm, $M_\infty = 2$, $T_\infty = 290$ K, $\bar{L} = 5$ cm, $\Delta x = \Delta y = 0.02$, $\bar{r}_p = 1.0$ μm . (b) Collection factor of a truncated cylinder, $M_\infty = 2$, $T_\infty = 290$ K, $\bar{L} = 5$ cm, $\Delta x = \Delta y = 0.02$.

on the frontal surface of the body to the radius of the frontal surface. The limiting particle streamlines are demonstrated in figure 18.

For a systematic analysis of the particle impaction on the body surface, several impaction parameters have been proposed previously (Forney & McGregor 1987). These parameters are essentially derived from the parameter Ψ defined in (24) by suitable rescaling. When there is a shock wave in front of the body or the free stream is supersonic, the choice of appropriate scaling parameters is very difficult. For example, Forney & McGregor (1987) have proposed the impaction parameter

$$\Psi = \Psi_r \left(\frac{\bar{L}}{\bar{\Delta}} \right), \tag{26}$$

where \bar{L} is the body radius and $\bar{\Delta}$ is the shock stand-off distance. Here Ψ_r is the impaction parameter for subsonic flow ($M \leq 0.4$) of Israel & Rosner (1983), which is given by

$$\Psi_r = \frac{4}{3} \left(\frac{\bar{\rho}_{mp}}{\bar{\rho}} \right) \left(\frac{2\bar{r}_p}{\bar{L}} \right) \Phi_c \int_0^{R_{ep}} \frac{dR_e}{C_D R_e}, \tag{27}$$

where R_{ep} is the particle Reynolds number ($= 2\bar{r}_p \bar{\rho} \Delta \bar{u}_p / \bar{\mu}$, $\Delta \bar{u}_p$ is the particle velocity relative to the gas) and Φ_c is the collection factor due to departure from the continuum flow of the gas around a particle.

The particle drag coefficient depends on three parameters: R_{ep} , M_p ($= \Delta \bar{u}_p / \bar{c}$) and T_p/T . The particle Knudsen number K_{np} is related to R_{ep} and M_p through $K_{np} = (\frac{1}{2}\pi\gamma)^{\frac{1}{2}} M_p / R_{ep}$. Then we can use the same procedure as Forney & McGregor (1987) to obtain the impaction parameter Ψ defined in (25) by approximating $T_p/T = 1$. The present results are plotted in figure 18(b), and compared with their theoretical results. the collection factor E_p seems to be correlated fairly well with the impaction parameter Ψ . However, the present results deviate from the theoretical curve obtained by Forney & McGregor (1987) for $\Psi^{\frac{1}{2}} < 0.8$. This discrepancy is however quite natural, because in their analysis, a thin-walled cylinder pipe is used and the gas is injected into the pipe inlet where the body surface would be placed in our study. This difference is very important for the particles with smaller impaction

parameters Ψ . The particles along the limiting particle streamline tend to follow very closely the gas flow near the body surface. The gas flow field in front of the thin-walled cylindrical probe for zero injection rate will not coincide with that in front of the truncated cylinder with a rigid surface.

Forney & McGregor (1987) suggest that the impaction parameter Ψ should be useful in attempts to predict the particle impaction on a variety of shapes suspended in supersonic streams. Their collection factor E'_p is defined by $(E_p - f)/(1 - f)$, where f is the injection rate and E_p is the collection factor for $f = 0$, and numerical results are well correlated with the impaction parameter Ψ . According to the definition of E'_p and their corresponding discussions, E'_p should be correlated with this impaction parameter Ψ independent of the injection rate f . This will mean that the present plot of E_p , which is given by E'_p for $f = 0$, against the impaction parameter $\Psi^{\frac{1}{2}}$ should be close to their theoretical curve. Our results, however, deviate from their curve for $\Psi^{\frac{1}{2}} < 0.8$. This fact suggests that Forney & McGregor's conclusion should be modified. The present results demonstrate that the collection factor E_p changes with a very steep slope to zero near $\Psi \approx 0.5$. Here it must be noticed that the residence time becomes infinitely large for particles flowing along stagnation streamlines whose radii are less than some critical value. These particles cannot reach the body surface in a finite time.

We turn now to a discussion of the effects of the gas viscosity on the collection factor E_p , which was neglected in the present study. As the particles become small, those that enter into the shock layer near the body axis flow through the gas flow field very close to the body surface. In an actual viscous flow, these particles would be significantly affected by the boundary layer. Whether the boundary layer is laminar or turbulent will be decisively important for the collection factor E_p of these small particles. This problem remains for future study.

4.3. Two-phase flow

In the calculations of gas-particle flows, the loading ratio ν is set to 0.3 for all flows. The numerical procedures are similar to those in the previous section. The one-phase results at the final time steps n in figures 5, 9 and 12(a) are used as the initial flow conditions. The particle clouds are injected into a gas flow successively at every time step n after initiation of the two-phase calculation. The properties of the particles in each cloud are set to those of the gas at the injected point. Since the gas and the particle phases interact with each other, both phases are always solved simultaneously.

At each step, the time interval Δt is first determined by the CFL condition for the gas-phase flow. This time interval Δt is used for the particle phase analysis, too.

The injection points of the clouds are distributed uniformly on the injection plane. The number of particles per unit depth of a cloud injected at $y = y_{pk}^*$ is given by

$$N_{pk}^* = \rho^* |u^*| \Delta y_{pk}^* \Delta t, \tag{28}$$

where the asterisk denotes the flow conditions at the injection point of the cloud and Δy_{pk}^* is the radial width of its cross-section. Note that the relation $n_p^* = \rho^*$ has been used in (28). Obviously

$$\left. \begin{aligned} & y_{p(k+1)}^* - y_{pk}^* = \Delta y_{pk}^*, & y_{p1}^* &= 0.5 \Delta y_{p1}^*, \\ \Sigma \Delta y_{pk}^* &= \begin{cases} 1 & \text{for jet flows,} \\ R \ (\approx 2.5) & \text{for a flow around a truncated cylinder,} \end{cases} \end{aligned} \right\} \tag{29}$$

must be satisfied, where R is the half-height of the computational domain. Here it must be remembered that N_{pk}^* is a function of the computational time t , because the time interval Δt determined by the CFL condition depends on the temporal flow conditions.

The number of clouds injected into a flow at each time step is always set to a constant. This number is denoted by K and is shown in the following figures. Since Δy_{pk}^* is chosen to be constant for all k , we can obtain Δy_{pk}^* from $1/K$ for jet flows and from R/K for a flow around a truncated cylinder. In all cases, this Δy_{pk}^* is chosen so small that the condition $\Delta y_{pk}^* \ll \Delta y$ is well satisfied. It is also automatically satisfied that $|u^*|\Delta t$ is much smaller than the mesh size Δx . Then $\Delta S_{pk}^* = \Delta y_{pk}^* |u^*| \Delta t$ is sufficiently small compared with the averaging area $S_p = \Delta x \Delta y$.

In the present analysis, it is implicitly assumed that ΔS_{pk} at a time t or a time step n is always much smaller than S_p . This can be checked only after the numerical results are obtained. As will be shown later, in the actual calculations, it is not easy to check whether this condition is completely satisfied for all particle clouds, when the flow field is unsteady. This is because local disintegration of a global particle cloud can occur owing to rapid changes of the gas flow field. In such a case, some isolated particle subclouds and also embedded dust-free regions may reasonably be expected to appear in the flow field.

A sonic jet of a gas-particle mixture expanded into a stagnant gas is shown in figure 4 for $\bar{r}_p = 1.0 \mu\text{m}$. By comparing the results with the corresponding dust-free ones, several important features of the gas-particle jet can be found. First, the spreading region of the dusty jet is much enlarged in the radial direction. The location of the Mach disk is shifted downstream and the strengths of the barrel shock and the Mach disk are reduced. The subsonic flow region surrounded by the jet boundary and the slip line downstream of the Mach disk becomes appreciably less spatially periodic. Furthermore, the fluctuating motion of the jet core downstream of the Mach disk, which is only subsonic in the jet, is effectively suppressed (see figure 19).

In the expansion region surrounded by the barrel shocks upstream of the Mach disk of the dust-free jet, the gas is accelerated and its temperature decreases rapidly with increasing axial distance. In the dusty jet, interactions between the gas and the particle phases tend to suppress the increase in gas velocity and the decrease in gas temperature. Then the Mach number of the gas is increased less effectively than in the dust-free jet. The maximum Mach number attained in the present dusty jet is nearly two-thirds of that in the corresponding dust-free jet. Hence the strength of the Mach disk is decreased.

The time history of the density profile along the jet axis is shown in figure 19. After initiation of the particle injection into the flow field, the location of the Mach disk is shifted downstream. The small-scale density fluctuations in the region downstream of the Mach disk diminish with increasing time step n . For n greater than about 2000 (+6000), the flow field downstream of the Mach disk is slightly oscillatory with time, and the relaxation region behind the Mach disk can be clearly observed.

The locations of centres of the particle clouds in the jet shown in figure 4 are given in figure 20. As far as the particle behaviour is concerned, any essential difference between the results for $\nu_j = 0$ and 0.3 cannot be found. Merely the scale of the fluctuation of streaklines is decreased with the increasing loading ratio. Particle streaklines are very smooth except in the subsonic region surrounded by the Mach disk and the slip lines. An extremely high concentration of particles is realized near the jet boundary. Fluctuation of the particle streaklines is appreciable in the subsonic

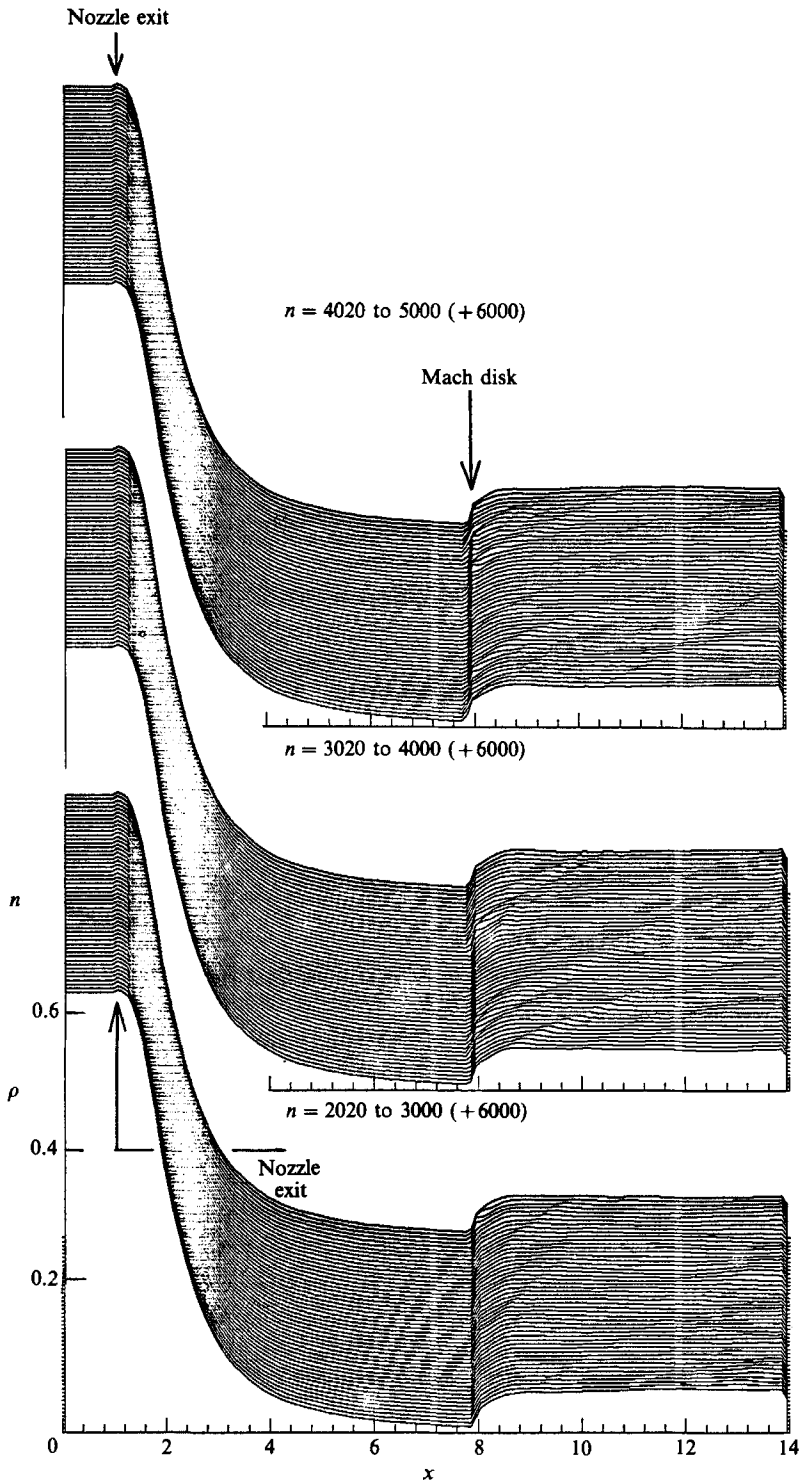


FIGURE 19. Time history of density profile along the jet axis of the two-phase jet shown in figure 4.

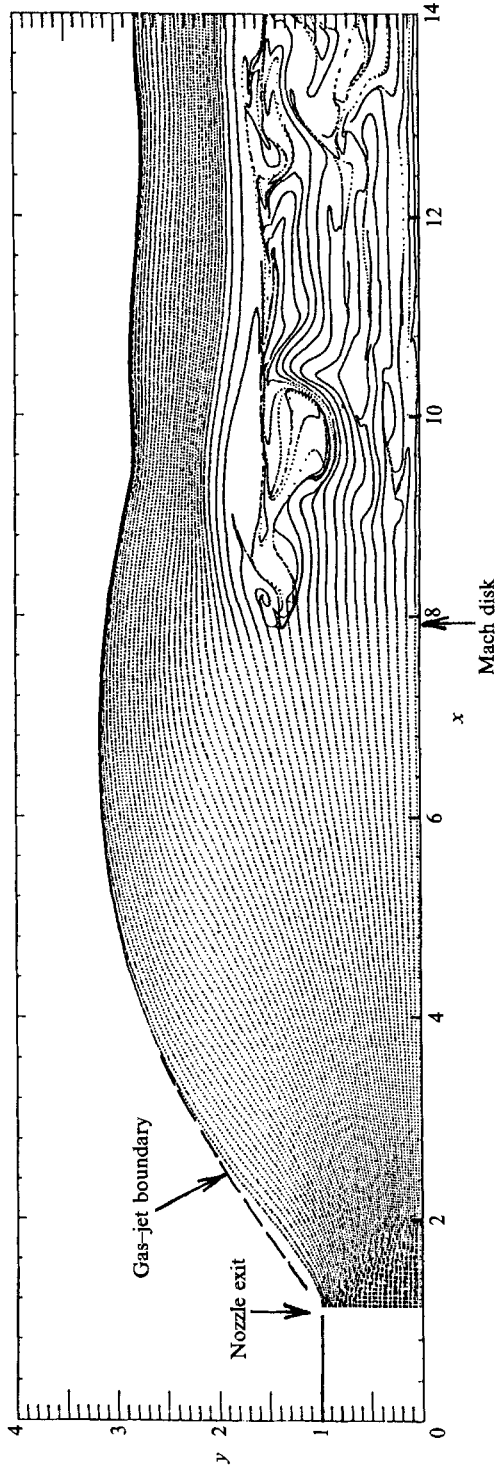


FIGURE 20. Locations of particle clouds in the jet shown in figure 4, $\Psi = 0.17$.

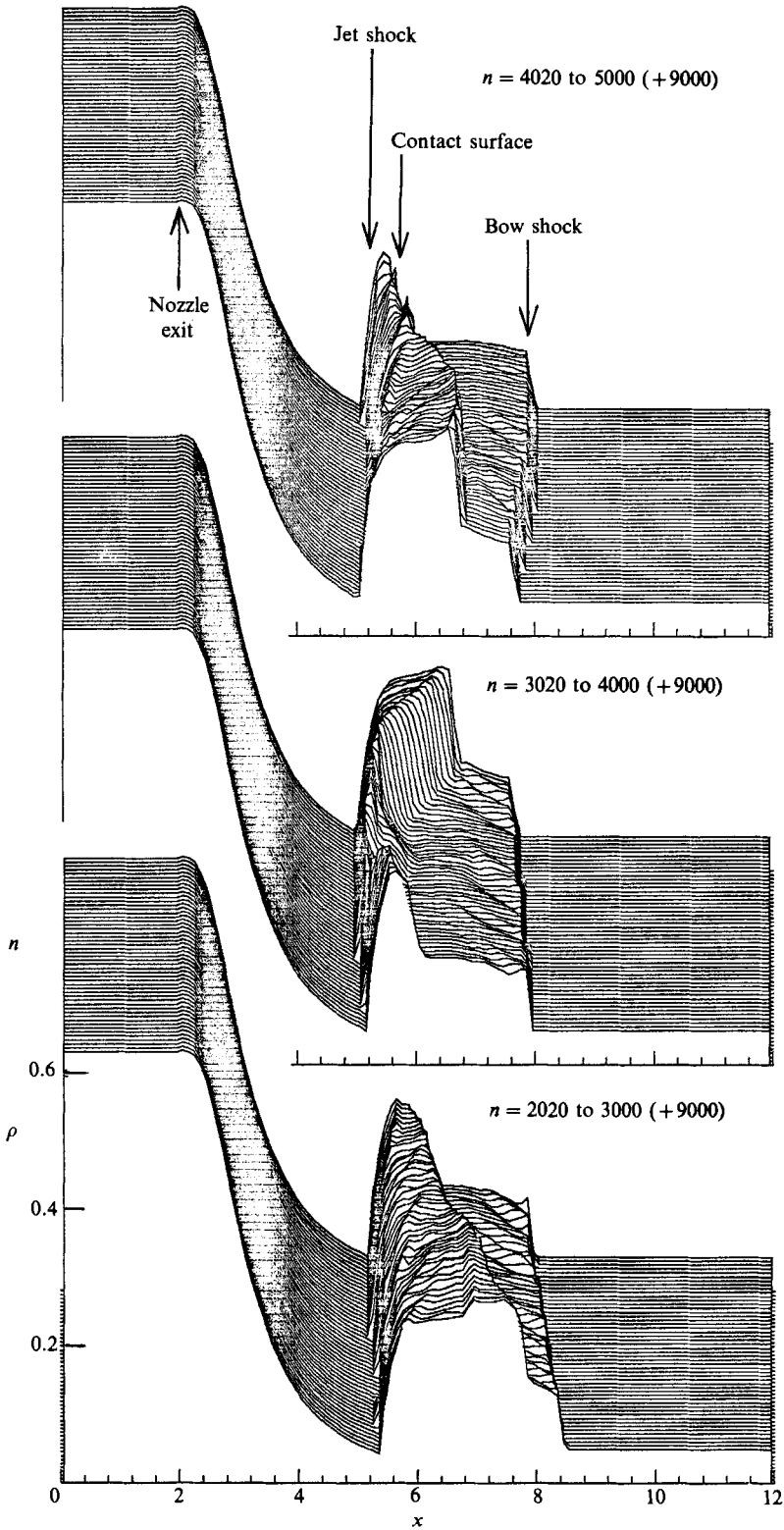


FIGURE 21. Time history of density profile along the jet axis of the two-phase jet shown in figure 8.

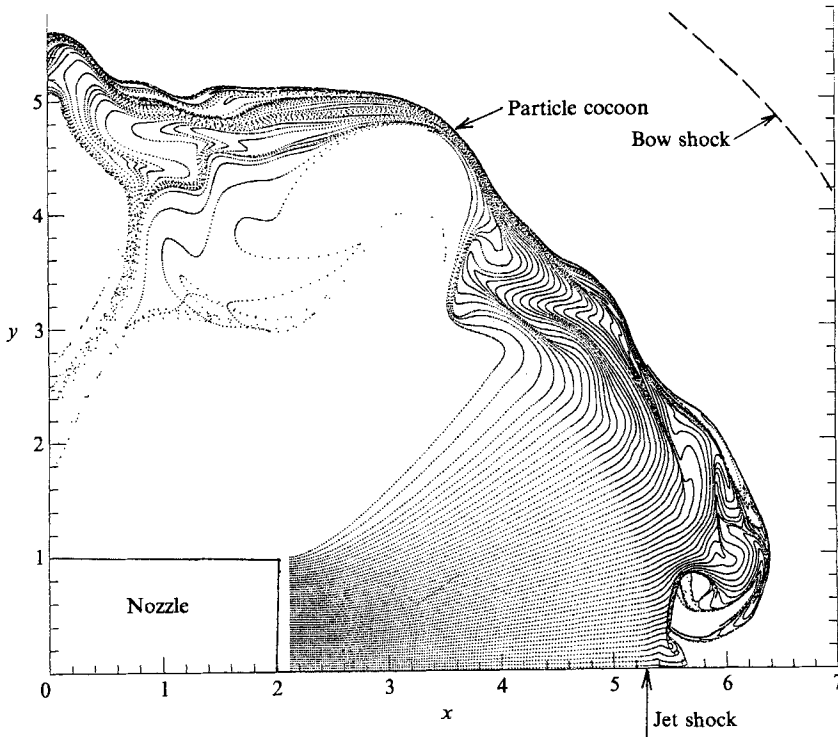


FIGURE 22. Locations of particle clouds in the jet shown in figure 8, $\Psi = 0.17$.

region downstream of the Mach disk even in the dusty jet. This fluctuation is clearly most prominent near the slip line.

A numerical result for a dusty opposing jet is shown in figure 8. As in the sonic jet expanded into a stagnant gas, the jet-shock distance from the nozzle exit plane is appreciably enlarged. This in turn results in a shift of the locations of the contact surface and the bow shock towards the jet exhaust direction. It is interesting that the shape of the bow shock differs slightly from that in the one-phase jet. Then the flow field in the region between the contact surface and the bow shock in the two-phase jet is similar to that in the one-phase jet.

One of the most important effects of the presence of particles is seen in the instability of the contact surface. This situation is well demonstrated in the time history of the density profile along the jet axis shown in figure 21. The location of the contact surface and the distance between the bow shock and the contact surface on the jet axis change more drastically than in the one-phase jet. In general, the presence of particles tends to suppress the flow instabilities which would appear in the corresponding one-phase flow. Thus the enhancement of instability of the contact surface found in the present result is an interesting example where the presence of particles tends to reinforce the instability. In the one-phase jet, the contact surface near the axis protrudes toward the bow shock. This situation is reversed in the two-phase result. This phenomenon itself is, however, not an essential difference between the one- and the two-phase jets. As is shown in the time history of the density profile along the jet axis (figures 9 and 21), the location of the contact surface depends on the time step n . The concave or the convex shape of the contact surface

near the jet axis appears almost periodically with time both in the one- and the two-phase jets.

The dusty region in the opposing jet is shown in figure 22. Compared with the results for $\nu_j = 0$, the particles travel larger distances in the flow field both in the axial and the radial directions. The radius of the outer wall of the particle cocoon becomes large and its behaviour becomes very complicated in the two-phase jet.

A supersonic two-phase flow around a truncated cylinder is shown in figure 11, where the particles impinging on the body surface are assumed to stick to or to be absorbed by the surface. As was discussed previously, if the particles that impinge on the body surface are reflected elastically, a particle sheet will appear in the flow field where the particle density ρ_p becomes infinitely large (see figure 17). In such a case, the assumption that the volume occupied by the particles is negligible will become invalid. Moreover, for small sizes of particles, a very large particle concentration will also be realized near the shoulder of the body surface (see figure 16). Thus the present calculation has been carried out for particles with radius $\bar{r}_p = 2.0 \mu\text{m}$ under the condition that the particles impinging on the body surface are absorbed by the body surface.

Numerically, a large number of particle clouds must be considered, because the radius of the computational domain R is set to 2.5 ($\bar{R} = 2.5\bar{L}$). This means that a large computer memory and also a large computing time are required in order to get a reliable numerical solution. Although the mesh size $\Delta x (= \Delta y)$ was chosen as 0.05 , the amount of computation increased to a significant degree. The VP ratio in our computer program is approximately 0.96 . In spite of this, one run required more than four hours on the VP-400 supercomputer.

The two-phase solution for $\bar{r}_p = 2.0 \mu\text{m}$ is shown in figure 11. In this case the one-phase solution was calculated for $1 \leq n \leq 4000$ and the particles were injected into the one-phase solution for $n \geq 4001$. In order to investigate in detail the time evolution of the shock layer, a space-time diagram of the density distribution along the axis is shown in figure 12(b). As was mentioned above, the flow is dust-free for $1 \leq n \leq 4000$ and dusty for $4001 \leq n \leq 8000$. The dust-free result shows that the calculated flow field is slightly oscillatory with time and substantially steady for $n > 2000$. After the initiation of particle injection, the shock stand-off distance begins to decrease, and for $n > 1000(+4000)$ the density field in the shock layer becomes somewhat oscillatory with time. The amplitude of this oscillation is largest just behind the shock front. In spite of the oscillatory fluctuation of the density profile in the shock layer, the location of the bow shock is quite stationary and also the density profile near the body surface is almost steady for $n > 2000(+4000)$.

The discrete treatment of the particle-phase flow will perhaps be responsible for the oscillatory fluctuation of the density distribution. The number of clouds contained in each cell will not be constant with time even for large n . This will in turn produce some time change in the flow properties behind the shock front and then oscillatory fluctuations in the shock layer. Such fluctuations can, however, be almost suppressed before they reach the body surface, because the particle density becomes very large near the body surface and these particles can effectively absorb the disturbances. As is shown in figure 12(b), the amplitude of the density oscillation in the shock layer is much smaller than the total increase in density due to the presence of particles. Then the present result is sufficient to draw quantitative as well as qualitative conclusions about the effects of the presence of particles on the flow field.

As is shown in figure 11(c), the contours of constant Mach number of the two-phase flow are very similar to those of the one-phase flow. However, comparing the results

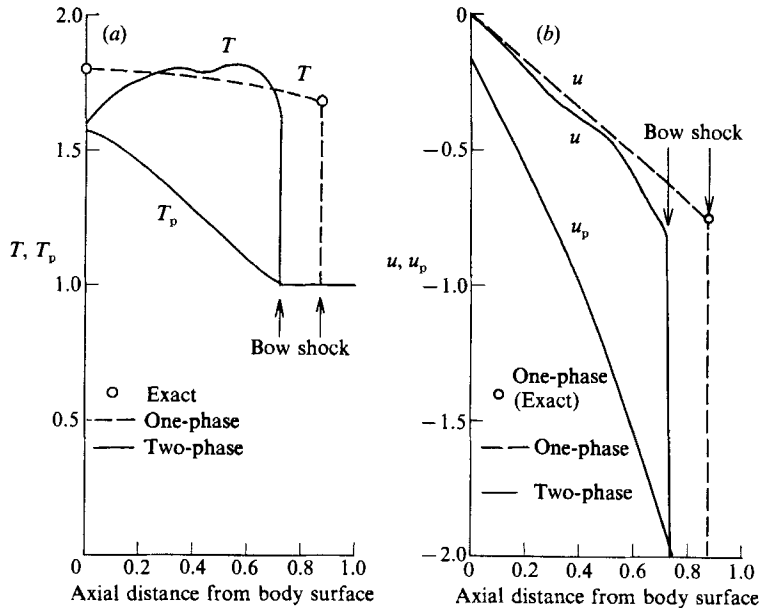


FIGURE 23. Axial distributions of gas and particle properties in the supersonic flows around a truncated cylinder shown in figure 11; (a) distributions of the gas and the particle temperatures; (b) distributions of the gas and the particle velocities.

with the dust-free ones, we find that the contours of constant density and pressure are very different from those of the one-phase flow.

In figure 23, distributions of the temperatures and the velocities of both the phases along the axis are shown. Some of the qualitative features of the two-phase flow are very similar to those obtained by Sugiyama (1983). The present results, however, show more complicated flow behaviour than his results. The shock stand-off distance of the two-phase flow is about 20% smaller than for the one-phase flow.

It should be noted that the shock wave obtained numerically by the finite-difference scheme using the Euler equations always has some finite thickness which is not the physical one. The particles begin to follow the change of the gas properties in this region, which leads to the fact that the gas properties just behind the shock front obtained numerically in the two-phase solution cannot exactly agree with the theoretical values, which are determined by the Rankine-Hugoniot relations under the assumption of a frozen shock front (see figure 23).

In the dusty shock layer, the gas temperature becomes highest at some point near the shock front. In the one-phase flow, the highest gas temperature is realized on the body surface. After the particles pass through the shock wave, the magnitude of the particle velocities decreases almost linearly along the axis and impinge on the body surface with some finite value.

In order to investigate the flow field of the particle phase, locations of the particle clouds are shown in figure 24. A dust-free region appears between the limiting particle streamline and the outer wall of the cylinder. In figure 18(a), the limiting particle streamline in the present two-phase flow is shown by a dashed line. Obviously, the effect of the presence of particles on the location of the limiting particle streamline is small. The collection parameter E_p and the impact parameter Ψ are 0.64 and 0.40, respectively. Although E_p is not affected appreciably by the particle loading ratio ν , Ψ depends on it rather strongly.

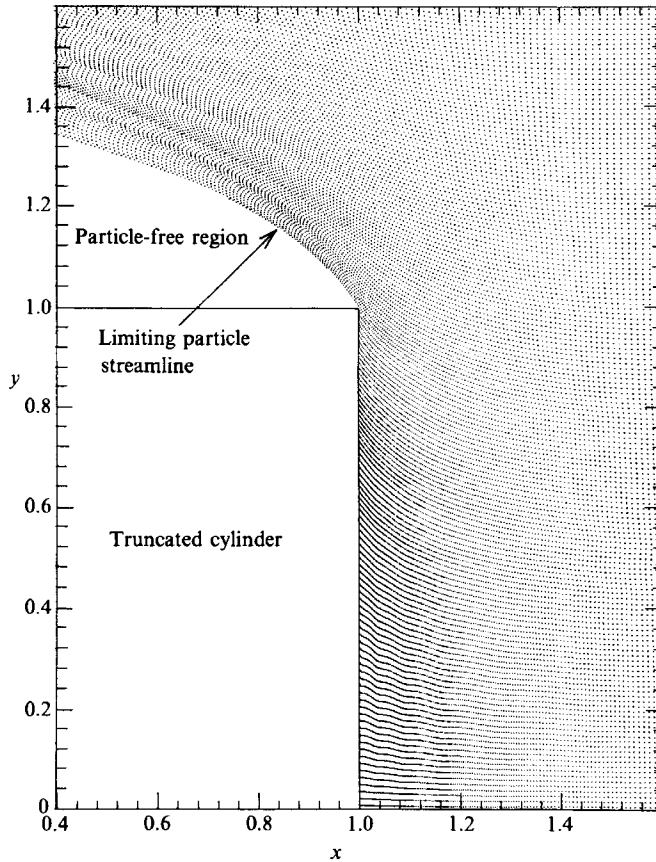


FIGURE 24. Locations of particle clouds in the flow shown in figure 11.

Since the present mesh is not aligned with the bow shock, some artificial disturbances are produced at the mesh interfaces on the bow shock (see figure 11). These disturbances affect the particle behaviour in the shock layer, which is responsible for a wavy pattern of the spatial distribution of the particle clouds near the limiting particle streamline. Moreover, because of the oscillatory motion of the flow field behind the bow shock, as was discussed previously, the particle streaklines in front of the body surface fluctuate a little.

Owing to the presence of the limiting streamline, characteristics of the two-phase flow in the dust-free region are appreciably different from those of the one-phase flow in the corresponding flow region. This can be recognized by comparing the one- and two-phase results in figure 11.

Finally, it is worth discussing the non-dimensional parameters characterizing the two-phase flows ($\nu > 0$). Since the two phases interact with each other, the flow field becomes much more complicated than the dust-free flow. The strength of the interaction can mainly be measured by the mass loading ratio ν . Moreover, the energy transfer between the two phases introduces an additional parameter $\theta = \bar{C}_{pp}/\bar{C}_{pg}$. Thus the non-dimensional parameters for the two-phase flows are Γ_τ , Γ_ρ , f_p , g_p , ν and θ in addition to the Mach number, the pressure ratio and possibly the density ratio of the gas-phase flow. These seem too many to expect that one or even a combination of a few universal parameters can characterize successfully the

two-phase flows. However, making effort to find these universal parameters will be very important at least from the engineering point of view. For this purpose, more detailed sample calculations will be necessary.

5. Conclusions

Sonic jets expanded into a stagnant gas, sonic jets opposing a supersonic main flow and supersonic flows of gas-particle mixtures around a truncated cylinder were calculated numerically by a time-dependent technique. The effects of the presence of the particles on the flow field were investigated in detail by comparing these results with the corresponding dust-free ones. Also, motions of dust particles in the gas flows were studied. It was confirmed that the particle motions become considerably complicated when strong discontinuities such as shock waves and slip lines and also a body surface are present in the flow field. In particular this situation is appreciably enhanced when the flow is not stationary. Disintegration of a large particle cloud because of some rapid change of the flow field may sometimes result in the production of small subclouds. Moreover, in some other situations, these particle subclouds coalesce or intersect to form multivalued regions of the particle properties.

A few of the universal parameters proposed previously, which characterize the particle motions in gas flows, were applied to the present study. Only in some simple situations were these successfully applied to correlate the particle motions. In general, however, it was almost impossible to correlate the particle behaviour with these parameters. This is because many strong discontinuities appear in the supersonic gas-phase flow. Then the gas conditions around the particles change very drastically during their passage through the gas flow field. Obviously some combinations of the parameters will be necessary to characterize the particle flow field, especially for two-phase flows with finite loading ratio.

Appendix. Piecewise-linear interpolation method

The piecewise-linear interpolation method (PLM) scheme is essentially a second-order sequel to Godunov's algorithm originally developed by Collella & Glaz (1983) and van Leer (1979), and has second-order accuracy in space and time. Since the governing equations (13) are first split into two sets of one-dimensional differential equations as in (18), it will be sufficient to describe this Riemann solver for a set of one-dimensional differential equations, here (18*a*). This is rewritten for simplicity in the form

$$\frac{\partial \mathbf{U}}{\partial t} + \frac{\partial \mathbf{F}}{\partial x} + \mathbf{H} = 0 \quad (\mathbf{H} = \mathbf{H}_x + \mathbf{H}_{px}), \quad (\text{A } 1)$$

which can also be rearranged into a different set,

$$\frac{\partial \mathbf{Q}}{\partial t} + \mathbf{A} \frac{\partial \mathbf{Q}}{\partial x} + \mathbf{C} = 0, \quad (\text{A } 2)$$

$$\frac{\partial v}{\partial t} + u \frac{\partial v}{\partial x} = 0. \quad (\text{A } 3)$$

Here \mathbf{Q} is a state vector defined by $\mathbf{Q} = (\rho, u, p)^T$ and \mathbf{A} is a matrix defined by $\partial \mathbf{F}' / \partial \mathbf{Q}$, where $\mathbf{F}' = (\rho, \rho u, e')^T$ and $e' = p / [\gamma(\gamma - 1)] + \frac{1}{2} \rho u^2$. The state vector \mathbf{C} is obtained in the transformation from (A 1) to (A 2) and (A 3).

Obviously the momentum equation in the y -direction, (A 3), is decoupled from the

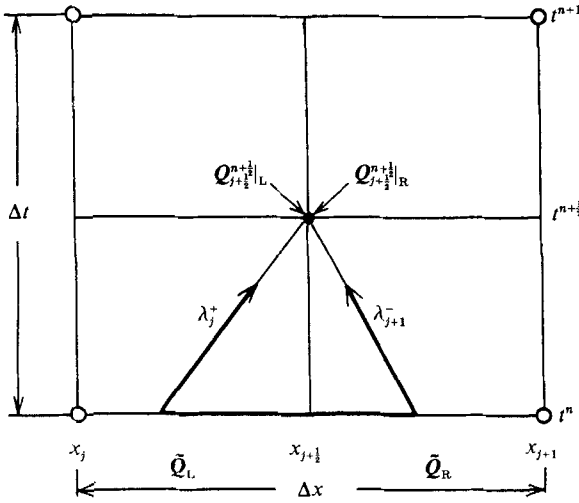


FIGURE 25. Scheme for the piecewise-linear interpolation method.

other equations and then the velocity component v can be determined independently after the set of equations (A 2) are solved. Then the problem is substantially reduced to the solution of a one-dimensional flow problem. In PLM, both forms of equations (A 1) and (A 2) and (A 3) are used in a unit process.

Referring to figure 25, grid points on a line parallel to the x -axis are designated by x_j ($j = 1, 2, 3, \dots$). The boundary between the j th and the $(j + 1)$ th zones is denoted by $x_{j+1/2}$ and the mesh size is defined by $\Delta x_j = x_{j+1/2} - x_{j-1/2}$. Since a uniform size of mesh is employed in the present analysis, we can put $\Delta x_j = \Delta x = \text{const}$. We assume that at time t^n we know U_j^n and wish to calculate U_j^{n+1} , the approximate solution at time t^{n+1} . The present second-order Godunov algorithm for doing so consists of the following four steps:

(i) The interpolated profiles for the primitive variables Q^n subject to the monotonicity constraints are obtained by

$$Q^n(x) = Q_j^n + \left(\frac{x - x_j}{\Delta x} \right) \Delta Q_j \quad \text{for } x_{j-1/2} \leq x \leq x_{j+1/2}. \quad (\text{A } 4)$$

Here ΔQ_j is defined with appropriate monotonicity constraints, for example, as

$$\Delta Q_j = \text{sgn}(DQ) \min(2|DQ^+|, 2|DQ^-|, |DQ|), \quad (\text{A } 5)$$

where

$$DQ^+ = Q_{j+1}^n - Q_j^n, \quad DQ^- = Q_j^n - Q_{j-1}^n, \quad DQ = \frac{1}{2}(DQ^+ + DQ^-). \quad (\text{A } 6)$$

(ii) The time-centred left and right states $Q_{j+1/2}^{n+1}|_L$ and $Q_{j+1/2}^{n+1}|_R$ at the cell boundary $x_{j+1/2}$ are constructed approximately as

$$\left. \begin{aligned} Q_{j+1/2}^{n+1}|_L &= \tilde{Q}_L + P_> (Q_j^n - \tilde{Q}_L) + P_> \left[\left(1 - \frac{\Delta t}{\Delta x} A_j \right)^{1/2} \Delta Q_j \right] - P_> \left(\frac{1}{2} \Delta t C_j \right), \\ Q_{j+1/2}^{n+1}|_R &= \tilde{Q}_R + P_< (Q_{j+1}^n - \tilde{Q}_R) - P_< \left[\left(1 + \frac{\Delta t}{\Delta x} A_{j+1} \right)^{1/2} \Delta Q_{j+1} \right] - P_< \left(\frac{1}{2} \Delta t C_{j+1} \right), \\ P_> W &= \sum_{\lambda^* > 0} (I_j^* W) r_j^*, \quad P_< W = \sum_{\lambda^* < 0} (I_{j+1}^* W) r_{j+1}^*, \end{aligned} \right\} \quad (\text{A } 7)$$

where $\lambda^*(\lambda^+ = u + c, \lambda^0 = u, \lambda^- = u - c)$ are the characteristic values of the matrix \mathbf{A} , \mathbf{l}^* and \mathbf{r}^* are the corresponding normalized left and right eigenvectors, respectively, and $\tilde{\mathbf{Q}}_L$ and $\tilde{\mathbf{Q}}_R$ are given by

$$\left. \begin{aligned} \tilde{\mathbf{Q}}_L &= \mathbf{Q}_j^n + \left[1 - \max(\lambda_j^+, 0) \frac{\Delta t}{\Delta x} \right] \frac{1}{2} \Delta \mathbf{Q}_j, \\ \tilde{\mathbf{Q}}_R &= \mathbf{Q}_{j+1}^n - \left[1 + \min(\lambda_{j+1}^-, 0) \frac{\Delta t}{\Delta x} \right] \frac{1}{2} \Delta \mathbf{Q}_{j+1} \end{aligned} \right\} \quad (\text{A } 8)$$

(see figure 25). In this step, governing equations in the form (A 2) are used.

(iii) The Riemann problem at the boundary $x_{j+\frac{1}{2}}$ with the left and right states of \mathbf{Q} obtained in step (ii) are solved to obtain $\mathbf{Q}_{j+\frac{1}{2}}^{n+\frac{1}{2}}$. In the present study, the Riemann problem is solved numerically by an iterative method proposed by Chorin (1976).

(iv) Equation (A 1) is used to get \mathbf{U}_j^{n+1} as

$$\mathbf{U}_j^{n+1} = \mathbf{U}_j^n + \frac{\Delta t}{\Delta x} (\mathbf{F}_{j-\frac{1}{2}} - \mathbf{F}_{j+\frac{1}{2}}) - \frac{1}{2} \Delta t (\mathbf{H}_{j-\frac{1}{2}} + \mathbf{H}_{j+\frac{1}{2}}), \quad (\text{A } 9)$$

where

$$\mathbf{F}_{j+\frac{1}{2}} = \mathbf{F}(\mathbf{U}(\mathbf{Q}_{j+\frac{1}{2}}^{n+\frac{1}{2}})) \text{ and } \mathbf{H}_{j+\frac{1}{2}} = \mathbf{H}(\mathbf{U}(\mathbf{Q}_{j+\frac{1}{2}}^{n+\frac{1}{2}}), \mathbf{U}_{pj+\frac{1}{2}}^{n+\frac{1}{2}}).$$

In all these steps, the particle quantities formally designated by $\mathbf{U}_{pj+\frac{1}{2}}^{n+\frac{1}{2}}$ are assumed to be known and fixed.

This scheme is the so-called second-order upwind scheme and so is numerically very robust in the analysis of supersonic flows with strong discontinuities such as shock waves and slip lines.

The authors would like to express their cordial thanks to Professors S. Morioka, N. Hatta and T. Matsuda for their valuable discussions and criticisms. The authors also acknowledge support through a Grant-in-Aid for Scientific Research (62613506) of the Ministry of Education and Culture in Japan.

REFERENCES

- CARLSON, D. J. & HOGLUND, R. F. 1973 Particle drag and heat transfer in rocket nozzles. *AIAA J.* **11**, 1980.
- CARRIER, G. F. 1958 Shock waves in a dusty gas. *J. Fluid Mech.* **4**, 376.
- CHORIN, A. J. 1976 Random choice solution of hyperbolic systems. *J. Comput. Phys.* **22**, 517.
- CHUNG, J. N. & TROUTT, T. R. 1988 Simulation of particle dispersion in an axisymmetric jet. *J. Fluid Mech.* **186**, 199.
- CHUSKIN, P. I. 1962 Investigation of flow round blunt bodies of revolution at supersonic velocities. *Zh. Vych. Mat. mat. Fiz.* **2**, 255.
- COLLELLA, P. & GLAZ, H. M. 1983 Efficient solution algorithm for the Riemann problem for real gases. *Lawrence Berkeley Laboratory-15776*.
- CROWE, C. T. 1982 Review - Numerical models for dilute gas-particle flows. *Trans ASME I: J. Fluids Engng* **104**, 297.
- FINLEY, P. J. 1966 Jet opposing a supersonic free stream. *J. Fluid Mech.* **26**, 337.
- FORNEY, L. J. & MCGREGOR, W. K. 1987 Particle sampling in supersonic streams with a thin-walled cylindrical probe. *AIAA J.* **25**, 1100.
- HEALY, J. V. 1970 Two-phase convex-type corner flows. *J. Fluid Mech.* **41**, 759.
- HENDERSON, C. B. 1976 Drag coefficient of spheres in continuum and rarefied flows. *AIAA J.* **14**, 259.
- ISHII, R. & MATSUHISA, H. 1983 Steady reflection, absorption and transmission of small disturbances by a screen of dusty gas. *J. Fluid Mech.* **130**, 259.

- ISHII, R. & UMEDA, Y. 1987 Nozzle flows of gas-particle mixtures. *Phys. Fluids* **30**, 752.
- ISRAEL, R. & ROSNER, D. E. 1983 Use of a generalized Stokes number to determine the aerodynamic capture efficiency of non-Stokesian particles from a compressible gas flow. *Aero. Sci. Technol.* **2**, 45.
- KENDALL, J. M. 1959 Experiments on supersonic blunt-body flows. *Jet. Prop. Lab. Progress Rep.* 20-372.
- KOBAYASHI, H., NAKAGAWA, T. & NISHIDA, M. 1984 Density measurements by laser interferometry. *Proc. Intl Symp. of RGD* (ed. H. Oguchi). University of Tokyo.
- KÖSSEL, D. & MÜLLER, E. 1988 Numerical simulation of astrophysical jets: the influence of boundary conditions and grid resolution. *Max-Planck-Institute Für Physik und Astrophysik* 340.
- LEER, VAN B. 1979 Towards the ultimate conservative difference scheme. V. A second-order sequel to Godunov's method. *J. Comput. Phys.* **32**, 101.
- LOVE, E. S., GRIGSBY, C. E., LEE, L. P. & ROBERTS, W. W. 1959 Experimental and theoretical studies of axisymmetric free jets. *NASA TN R-6*.
- MARBLE, F. E. 1963 Nozzle contours for minimum particle-lag loss. *AIAA J.* **12**, 2793.
- MARBLE, F. E. 1970 Dynamics of dusty gases. *Ann. Rev. Fluid Mech.* **2**, 397.
- MATSUDA, T., UMEDA, Y., ISHII, R., YASUDA, A. & SAWADA, K. 1987 Numerical and experimental studies on choked underexpanded jets. *AIAA Paper* 87-1378.
- MAXEY, M. R. & RILEY, J. J. 1983 Equation of motion for a small rigid sphere in a nonuniform flow. *Phys. Fluids* **26**, 883.
- MICHAEL, D. H. & NOREY, P. W. 1969 Particle collision efficiency for a sphere. *J. Fluid Mech.* **37**, 565.
- MORSI, S. A. & ALEXANDER, A. J. 1969 An investigation of particle trajectories in two-phase flow systems. *J. Fluid Mech.* **55**, 193.
- NORMAN, M. L., SMARR, L., WINKLER, K. H. A. & SMITH, M. D. 1982 Structure and dynamics of supersonic jets. *Astron. Astrophys.* **113**, 285.
- POWELL, A. 1953 On the mechanism of choked jet noise. *Proc. Phys. Soc. B* **66**, 1039.
- PROBSTEIN, R. F. & FASSIO, F. 1970 Dusty hypersonic flows. *AIAA J.* **8**, 772.
- ROMEO, P. J. & STERRETT, J. R. 1963 Exploratory investigation of the effect of a forward-facing jet in the bow shock of a blunt body in a Mach number 6 free stream. *NASA TN D-1605*.
- ROMEO, P. J. & STERRETT, J. R. 1965 Flow fluid for sonic jet exhausting counter to a hypersonic mainstream. *AIAA J.* **3**, 544.
- RUDINGER, G. 1969 *Nonequilibrium Flows*, vol. 1, p. 119. Dekker.
- SAFFMAN, P. G. 1965 The lift on a small sphere in a slow shear flow. *J. Fluid Mech.* **22**, 385.
- SCHMITT-VON SCHUBERT, B. 1969 Existence and uniqueness of normal shock waves in gas-particle mixtures. *J. Fluid Mech.* **38**, 633.
- SUGIYAMA, H. 1983 Numerical analysis of dusty supersonic flow past blunt axisymmetric bodies. *University of Toronto, Institute for Aerospace Studies. Rep.* 267.
- TAM, C. K. 1969 On the noise of a nearly ideally expanded supersonic jet. *J. Fluid Mech.* **38**, 537.
- TAM, K. W. T. 1972 The drag on a cloud of spherical particles in low Reynolds number flow. *J. Fluid Mech.* **51**, 69.
- UMEDA, Y., MAEDA, H. & ISHII, R. 1987 Discrete tones generated by the impingement of a high-speed jet on a circular cylinder. *Phys. Fluids* **30**, 2380.
- VAN DYKE, M. D. 1958 A model of supersonic flow past blunt axisymmetric bodies, with application to Chester's solution. *J. Fluid Mech.* **3**, 515.
- ZUCROW, M. J. & HOFFMAN, J. P. 1977 *Gas Dynamics*, vol. 2, p. 269. Wiley.